CALCULATION OF SOLAR WIND FLOWS ABOUT TERRESTRIAL PLANETS

by

Stephen S. Stahara
John P. Spreiter

NEAR TR 262

August 1982

Prepared under Contract No. NASW-3184

for

National Aeronautics & Space Administration
Washington, D. C. 20546

by

Nielsen Engineering & Research, Inc.
510 Clyde Avenue, Mountain View, CA 94043
Telephone (415) 968-9457

CONTENTS

1. Report No.	2. Government Accession No.	3. Recipient's Catalog No.

4. Title and Subtitle	5. Report Date
Calculation of Solar Wind Flows About Terrestrial Planets	6. Performing Organization Code 494/C

7. Author(s)	8. Performing Organization Report No.
Stephen S. Stahara and John R. Spreiter	NEAR TR

9. Performing Organization Name and Address	10. Work Unit No.
Nielsen Engineering & Research, Inc. 510 Clyde Avenue Mountain View, California 94043	11. Contract or Grant No. NASW-3184

12. Sponsoring Agency Name and Address	13. Type of Report and Period Covered Contractor Report 7/78 - 12/81
National Aeronautics and Space Administration Washington, D. C. 20546	14. Sponsoring Agency Code

15. Supplementary Notes

16. Abstract

A summary report is provided of the work performed under NASA Contract No. NASW-3184. This work relates to the development of a computational model for the determination of the plasma and magnetic field properties of the global interaction of the solar wind with terrestrial planetary magneto/ionospheres. The theoretical method is based on an established single fluid, steady, dissipationless, magnetohydrodynamic continuum model, and is appropriate for the calculation of supersonic, super-Alfvénic solar wind flow past terrestrial planets. Provided in the report is a concise statement of the problems studied, a summary of the important research results, and copies of the publications.

17. Key Words (Suggested by Author(s))	18. Distribution Statement
solar-wind/planetary interaction frozen magnetic field	Unclassified-Unlimited Subject category 92

19. Security Classif. (of this report)	20. Security Classif. (of this page)	21. No. of Pages	22. Price*
Unclassified	Unclassified		

*For sale by the National Technical Information Service, Springfield, Virginia 22161

CALCULATION OF SOLAR WIND FLOWS ABOUT TERRESTRIAL PLANETS

Stephen S. Stahara
John R. Spreiter

I. INTRODUCTION

This is the final summary report under Contract No. NASW-3184 for the National Aeronautics and Space Administration. All of the important results of the research performed under this contract have been reported in the open literature, both in scientific journals and as technical papers at scientific meetings, with appropriate acknowledgements to NASA support. This summary report provides a statement of the problem studied, a descriptive summary of the most important results, a reference list and copies of all publications resulting from the research, and a list of all participating scientific personnel.

2. STATEMENT OF PROBLEM STUDIED

The problem toward which the research under this contract was directed was the modeling of the three-dimensional global interaction of the solar wind with terrestrial planet magneto/ionospheres. This was to be accomplished based on a continuum rather than particle viewpoint. The theoretical method employed is based on an established single fluid, steady, dissipationless magnetohydrodynamic model that is appropriate for the calculation of supersonic, super-Alfvénic solar wind flow past magneto/ionopause obstacle shapes typical of terrestrial planets. The overall objective was the enablement of rational modeling studies to be performed on the global solar wind interaction problem for the Earth and other terrestrial planets. This would involve the development and utilization of a multi-facited computational procedure that embodies the theoretical model

and incorporates advanced numerical methods so as to enable more general and detailed studies to be performed than heretofore possible. Comparisons of predictions from the model were anticipated both with existing theories where possible and with observational results where available. Additionally, the model was to be employed in several collaborative efforts with other space scientists in which predictions from the model would both augment other theoretical analysis and assist in interpreting results and comparisons with observations.

3. SUMMARY OF IMPORTANT RESEARCH RESULTS

The important results obtained under this contract are as follows.

3.1 Development and Verification of the Basic Procedure for Predicting the Global Plasma and Field Properties of the Three-Dimensional Solar Wind Flow Past Terrestrial Planet Magneto/Ionopause Obstacle Shapes

The basic theoretical model for predicting the global interaction of the solar wind with terrestrial planet magneto/ionospheres involves solution of the continuum partial differential equations of magnetohydrodynamics of a perfect gas having infinite electrical conductivity and zero viscosity and thermal conductivity which express the conservation of mass, momentum, energy, and magnetic field. The computational method developed to solve these equations is described in detail in ref. 1. Briefly, two separate finite-difference procedures are employed; one to treat the flow domain encompassing the bow shock and obstacle back to the terminator, and another to treat the flow domain downstream of the terminator. The reasons for doing this are discussed in ref. 1. The result is the achievement of a computational efficiency not possible by any other existing means.

One of the fundamental tasks of this part of the study was verification of the accuracy and range of validity of the computational procedure. This verification was accomplished through comparisons with other theoretical methods, and also by exercising the procedure on computations for obstacle shapes and solar wind flow conditions that span the entire range of interest of applications to terrestrial planets within the solar system. These results are reported in ref. 1 and demonstrate both the accuracy and robustness of the procedures.

Finally, one of the most significant achievements of the program was the incorporation of the entire computational procedure embodying the theoretical method into a modular, completely automated, user-friendly code. This permits any general user access to the results of the model at very reasonable computational cost. This feature of the effort is demonstrated in ref. 1 where examples are provided of detailed maps of the global interaction region for all important plasma and field variables.

3.2 Further Development and Evaluation of the Predictive Model by Detailed Comparisons of Plasma and Field Properties with Observational Data

The advanced computational model that was developed above was further refined and generalized. These developments related to both obstacle shape geometry and oncoming solar wind conditions and are detailed below.

A new family of obstacle shapes for solar wind/ionospheric interactions were determined which take account of gravitational variation in the scale height. These results are reported in ref. 2. A catalog of solar wind flows past these new shapes were obtained and results are presented in ref. 8. This catalog proved instrumental to a wide number of investigators engaged in related solar wind studies.

A significant refinement included in the computational model under this task has been the allowance of an arbitrary oncoming direction of the interplanetary solar wind. This refinement is detailed in ref. 2. This feature has been instrumental in showing that the asymmetry of the bow shock at the Earth previously observed and attributed to magnetic effects is either non-existent or at a level below that measurable by current spacecraft instrumentation. These and extensive related results employing the computational procecures which further demonstrate the accuracy of the predictive model are reported in refs. 4 and 5.

Finally, a provision for the determination of time histories of plasma and field properties along an arbitrary spacecraft trajectory has been incorporated into the computational model. This feature has proved invaluable in providing theoretical results for direct comparisons with spacecraft observations. Details of this provision and results of time history comparisons with plasma and field data from the Pioneer-Venus spacecraft are provided in ref. 2. In particular, comparisons with magnetic field observations for several orbits at quiet-time conditions are given and display very good agreement. Because determination of the frozen magnetic field is the last step in the computational model, its accurate prediction serves as a critical test of the correctness and accuracy of the theoretical and computational models.

3.3 Collaborative Efforts Employing Present Predictive Model

A number of collaborative efforts have been undertaken with other space scientists in which predictions from the present model have been employed to interprete observational results as well as to augment other theoretical analyses. The most extensive of these efforts has been with Dr. James A. Slavin and Prof. R. E. Holzer at the Institute of Geophysics

and Planetary Physics, UCLA. Results from the current predictive model provided the theoretical basis of an examination of solar wind flows past all the terrestrial planets. This was applied, first, to modeling the mean bow shock shape and its position and is reported in ref. 4; and then to interpreting these comparisons in light of both observations and previous analyses (ref. 5). The results from this study reported in refs. 4 and 5 represent the most detailed and comprehensive study to date of the global interaction phenomena of the solar wind with terrestrial planets, from the aspect of observations of the bow shock position and shape. They both confirm and verify the model's applicability to all terrestrial planets.

Another collaborative effort employing the current predictive model was carried out with John D. Mihalov of the Space Sciences Division at Ames Research Center. In that effort, which formed the basis of Mr. Mihalov's dissertation for Engineer's Degree from Stanford University, the predictive model was employed in a series of calculations involving time histories of detailed plasma and magnetic field properties in the ionosheath region of Venus, and comparisons thereof with observations from the Pioneer-Venus orbiter. These results are reported in ref. 6 and also indicate the correctness of the present model.

Finally, additional efforts have been underway with Ms. Nancy Crooker of UCLA regarding ISEE observations, Dr. William Knudsen of Lockheed Palo Alto Research Labs regarding Pioneer-Venus velocity potential analyzer observations and interpretations of the Venusian ionopause, and Dr. Janet Luhmann of UCLA regarding magnetic field draping observations at Venus.

3.4 References

1. Spreiter, J. R. and Stahara, S. S.: A New Predictive Model for Determining Solar Wind - Terrestrial Planet Interactions. Jour. of Geophy. Res., Vol. 85, No. A12, pp. 6769-6777, Dec. 1, 1980.

2. Spreiter, J. R. and Stahara, S. S.: Solar Wind Past Venus: Theory and Comparisons. Jour. of Geophy. Res., Vol. 85, No. A 13, pp. 7715-7738, Dec. 30, 1980.

3. Stahara, S. S., Klenke, D., Trudinger, B. C., and Spreiter, J. R.: Application of Advanced Computational Procedures for Modeling Solar-Wind Interactions with Venus - Theory and Computer Code. NASA CR 3267, May 1980.

4. Slavin, J. A. and Holzer, R. E.: Solar Wind Flow About the Terrestrial Planets 1. Modeling Bow Shock Position and Shape. Jour. of Geophy. Res., Vol. 86, No. A13, pp. 11,401-11,418, Dec. 1, 1981.

5. Slavin, J. A., Holzer, R. E., Spreiter, J. R., and Stahara, S. S.: Solar Wind Flow About the Terrestrial Planets 2. Comparison with Gasdynamic Theory and Implications for Solar-Planetary Interactions. Submitted to Jour. of Geophy. Res., Nov. 1981.

6. Mihalov, J. D.: Comparison of Gas Dynamic Model for Solar Wind Flow Around Venus with Pioneer Venus Orbiter Data. Stanford University Engineers Thesis, May 1981.

4. PUBLICATIONS LIST

1. Spreiter, J. R. and Stahara, S. S.: A New Predictive Model for Determining Solar Wind - Terrestrial Planet Interactions. Jour. of Geophy. Res., Vol. 85, No. A12, pp. 6769-6777, Dec. 1, 1980.

2. Spreiter, J. R. and Stahara, S. S.: Solar Wind Past Venus: Theory and Comparisons. Jour. of Geophys. Res., Vol. 85, No. A 13, pp. 7715-7738, Dec. 80, 1980.

Copies of these publications are provided in the Appendix.

5. LIST OF PARTICIPATING SCIENTIFIC PERSONNEL

(i) John R. Spreiter - Principal Investigator

(ii) Stephen S. Stahara - Co-Principal Investigator

APPENDIX

JOURNAL OF GEOPHYSICAL RESEARCH, VOL. 85, NO. A12, PAGES 6769-6777, DECEMBER 1, 1980

A NEW PREDICTIVE MODEL FOR DETERMINING SOLAR WIND-TERRESTRIAL PLANET INTERACTIONS

John R. Spreiter

Division of Applied Mechanics, Stanford University, Stanford, California 94305

Stephen S. Stahara

Nielsen Engineering & Research, Mountain View, California 94043

Abstract. A computational model has been developed for the determination of the gasdynamic and magnetic field properties of the solar wind flow around a magnetic planet, such as the earth, or a nonmagnetic planet, such as Venus. The procedures are based on an established single-fluid, steady, dissipationless, magnetogasdynamic model and are appropriate for the calculation of axisymmetric, supersonic, super-Alfvénic solar wind flow past a planetary magneto/ionosphere. Sample results are reported for a variety of solar wind and planetary conditions. Some of these are new applications; others are included to show that the new procedures produce the same results as previous procedures when applied to the same conditions. The new methods are completely automated and much more efficient and versatile than those employed heretofore.

Introduction

The magnetogasdynamic model for the interaction of the solar wind and a planetary magnetosphere, or ionosphere if the planet is nonmagnetic, has been found to be of great utility in the prediction and interpretation of observations in space. The development of this model has a long history stemming from the work of Spreiter and Jones [1963], Dryer and Faye-Petersen [1964, 1966], Spreiter and Summers [1966], Alksne [1967], Dryer and Heckman [1967], Spreiter et al. [1968, 1970], Alksne and Webster [1970], Spreiter and Alksne [1969, 1970], and Spreiter and Rizzi [1974]. Although the usefulness of the original results is well established, there is much to be desired. Results have been calculated for only a limited set of solar wind and planetary conditions. Moreover, the original solutions bordered on what was barely possible at the time, required considerable hand computation, and were extremely laborious. Improvements in both numerical methods and computer capabilities have now rendered such procedures thoroughly obsolete, both from the standpoint of efficiency of calculation and generality of application.

To remedy this situation, a new, efficient procedure has been developed that provides the numerical solution for the streamlines, magnetic field lines, and contours of density, speed, temperature, and magnetic field intensity similar to those familiar from the original literature. The basic theoretical model employed is that described by Spreiter, Alksne, and their colleagues in the work cited above. The present solution makes full use of recent advances in nonlinear computational fluid dynamics. These advances include an algorithm of Beam and Warming [1976] to determine the gasdynamic flow near the nose of the magneto/ionopause. The remainder of the flow field is calculated by using a method developed by Kutler et al. [1973] and by Chaussee et al. [1975]. The magnetic field is also calculated quite differently than it was previously, being based on the decomposition of Alksne and Webster [1970]. This paper presents an outline of the principal features of the analysis and a sample of the results. Complete details of the computational procedures are provided by Stahara et al. [1977].

Mathematical Model

The fundamental assumption of the present work and all of the geophysical work cited above is that the average bulk properties of solar wind flow around a planetary magneto/ionosphere can be described adequately by solutions of the continuum equations of magnetogasdynamics of a perfect gas having infinite electrical conductivity and zero viscosity and thermal conductivity. These equations, which express the conservation of mass, momentum, energy, and magnetic field, are given by the following expressions:

$$\frac{\partial \rho}{\partial t} + \frac{\partial}{\partial x_k}(\rho V_k) = 0 \tag{1}$$

$$\frac{\partial}{\partial t}(\rho V_i) + \frac{\partial}{\partial x_k}\left(\rho V_i V_k + p\delta_{ik} - \frac{B_i B_k}{4\pi} + \frac{B^2}{8\pi}\delta_{ik} + \frac{g_i g_k}{4\pi G} - \frac{g^2}{8\pi G}\delta_{ik}\right) = 0 \tag{2}$$

$$\frac{\partial}{\partial t}\left(\frac{\rho V^2}{2} + \rho e + \rho\phi + \frac{B^2}{8\pi}\right) + \frac{\partial}{\partial x_k}\left[\rho V_k\left(\frac{\rho V^2}{2} + e + \frac{p}{\rho} + \phi\right) + S_k\right] = 0 \tag{3}$$

$$\frac{\partial B_i}{\partial t} = \frac{\partial}{\partial x_k}(V_i B_k - V_k B_i), \qquad \frac{\partial B_i}{\partial x_i} = 0 \tag{4}$$

where

$$g_i = \frac{\partial \phi}{\partial x_i}, \qquad S_k = \frac{1}{4\pi}(V_k B^2 - B_k V_i B_i) \tag{5}$$

and the equation of state of a perfect gas is given by

$$p = \frac{\rho R T}{\mu} \tag{6}$$

Paper number 80A1121.
0148-0227/80/080A1121$01.00

In accordance with standard usage the symbols ρ, p, $\underset{\sim}{V}$, T, $e = C_v T$, and $h = e + p/\rho = C_p T$ refer to the density, pressure, velocity, temperature, internal energy, and enthalpy; C_v and C_p refer to the specific heats at constant volume and pressure; $R = (C_p - C_v)\mu = 8.31 \times 10^7$ ergs/g °K is the universal gas constant, and μ represents the mean molecular weight nondimensionalized so that $\mu = 16$ for atomic oxygen. For fully ionized hydrogen, μ is thus 1/2. The magnetic field $\underset{\sim}{B}$ and the Poynting vector $\underset{\sim}{S}$ for the flux of electromagnetic energy are in Gaussian units. The gravitational potential ϕ and acceleration $\underset{\sim}{g}$ are assumed to be due to massive fixed bodies so that their time derivatives are zero. Because of the omission of dissipative terms in these equations, surfaces of discontinuity may develop in the solution, across which the fluid and magnetic properties change abruptly, but in such a way that mass, momentum, magnetic flux, and energy are conserved. These are approximations to comparatively thin layers across which similar changes in the fluid and magnetic properties occur in the corresponding theory of a dissipative gas and correspond physically to the bow wave, magneto/ionosphere boundary, and possible other thin regions of rapidly changing properties.

The shape of the magneto/ionospheric obstacle, assumed to be axisymmetric about a line through the planet center extending parallel to the free-stream solar wind velocity vector, may be specified in either of two ways: by a numerical table of coordinates or by use of simplified models from the cited references, which enable the calculation of approximate magneto/ionopause shapes upon specification of a small number of solar wind and planetary magnetic field or ionospheric parameters.

For the earth or other magnetic planets having a dipole field this shape is obtained by rotating the equatorial trace of the three-dimensional magnetosphere surface determined by balancing the Newtonian pressure $p = K\rho_\infty V_\infty^2 \cos^2\psi_o$ against the magnetic pressure due to $2f$ times the tangential component of the dipole field. Here, K and f are constants usually taken to be unity (see Spreiter [1976] for a discussion), ρ and V are the density and velocity of the solar wind, the subscript ∞ refers to conditions in the incident stream upstream of the bow wave, and ψ_o is the angle between $\underset{\sim}{V}_\infty$ and the normal to the magnetopause. These considerations lead to the following differential equation for the geocentric distance to the magnetopause r_m as a function of geomagnetic longitude ϕ, measured in such a way that ϕ is equal to $\pi/2$ at the magnetosphere nose and increases to $3\pi/2$ as one moves around the flank of the magnetosphere to the remote tail [Beard, 1960]:

$$\frac{d\bar{r}_m}{d\phi} = r_m \left[\frac{\bar{r}_m^6 \sin\phi \cos\phi + \sqrt{\bar{r}_m^6 - 1}}{\bar{r}_m^6 \cos^2\phi - 1} \right] \qquad (7)$$

$$\pi/2 \le \phi \le 3\pi/2$$

In this equation, $\bar{r}_m = r_m/D$, $D = a_e (f^2 B_{eq}^2 / 2\pi K \rho_\infty V_\infty^2)^{1/6}$ is the geocentric distance to the magnetosphere nose, where a_e refers to the radius of the earth, and B_{eq} is the average intensity of the field at the geomagnetic equator.

For a nonmagnetic planet having a sufficiently dense ionosphere to withhold the solar wind, such as Venus appears to be most of the time, the ionopause shape is determined by balancing the Newtonian pressure and the ionospheric pressure approximated by

$$p = p_R \exp\left(-\frac{r - r_R}{H}\right) \qquad (8)$$

derived from (1)-(3) by assuming steady conditions, negligible velocity and magnetic field, and a constant ionospheric scale height $H = kT/mg$, where $k = 1.38 \times 10^{-16}$ ergs/°K is Boltzmann's constant, m is the mean molecular mass, and p_R is the pressure at some reference radius r_R. These considerations lead to the following differential equation for the coordinates r_i of the ionopause as a function of angle β from the ionopause nose as measured at the planetary center [Spreiter et al., 1970]:

$$\frac{dr_i}{d\beta} = r_i \left[\frac{\sin 2\beta - 2\sqrt{\Delta - \Delta^2}}{2(\Delta - \sin^2\beta)} \right] \qquad 0 \le \beta \le \pi \qquad (9)$$

in which $\Delta = \exp[-(r_i - R_o)/H]$, where R_o is the value of r_i at the ionopause nose where $\beta = 0$. A family of ionopause shapes can be obtained by integrating (9) for different values of H/R_o. Appropriate values of H/R_o for application to Venus and Mars appear to be in the range from 0.01 to 0.30.

Two important parameters which characterize the solar wind flow in the magnetogasdynamic model are the free-stream values for the Mach number $M = V/a$ and the Alfvén Mach number $M_A = V/A$, in which $a = (\gamma p/\rho)^{1/2}$ is the speed of sound, A is the Alfvén speed $A = (B^2/4\pi\rho)^{1/2}$, and γ is the ratio of specific heats, usually taken to be 5/3 in solar wind applications. Because M_{A_∞} is typically greater than 5 in the solar wind, an important simplification may be introduced on the basis that for large M_{A_∞} the magnetic terms in the momentum and energy equations (2) and (3) are generally sufficiently small compared with the gasdynamic terms that they may be disregarded therein. This decouples the solution for the fluid motion from the magnetic field, which may be calculated subsequently by using the induction equation (4) and values for $\underset{\sim}{V}$ already calculated.

Although few detailed comparisons have been made, other than those of Spreiter and Rizzi [1974], which made use of their complete magnetogasdynamic numerical solution for the special case of aligned flow, it is generally regarded that the magnetic field calculated in this way reproduces the broad characteristics of observations. However, the process indicates magnetic field strengths that may be too large immediately outside the magnetopause. Zwan and Wolf [1976] have made an interesting analysis of conditions in this region and concluded that the strong

magnetic fields would drive the plasma out along the field lines and produce a thin region of depleted plasma density. Crooker and Siscoe [1977] have shown further that an observed anisotropy of the magnetosheath pressure occurs naturally from a mirror instability of the resulting flow along the magnetic flux tubes. Neither of these properties nor any representation of the long discussed possibility of magnetic merging at the magnetopause are captured by the present model, but the ready ability to generate our solutions for any specified conditions should aid in further study of such phenomena.

Calculation of the Gasdynamic Flow Properties

The gasdynamic equations for supersonic flow past a blunt-nosed obstacle representative of a planetary magneto/ionosphere are solved most effectively by using one method for the nose region, where the flow accelerates from subsonic to supersonic speeds, and another for the remaining region, where the flow is purely supersonic. In the present work the solution for the nose region is calculated by using a new axisymmetric implicit unsteady Euler equation solver (IMP), which determines the steady state solution by a time-marching procedure. The remainder of the solution is calculated by using a shock-capturing marching procedure (SCT), which spatially advances the solution downstream as far as required by solving the steady Euler equations.

Implicit Unsteady Euler Equation Solution for the Nose Region

The partial differential equations employed in the implicit code are the unsteady gasdynamic Euler equations derived from (1)-(3) by deleting the magnetic and gravitational terms and specializing for axisymmetric flows. Upon introduction of the generalized independent variable transformation $\tau = T$, $\xi = \xi(T,X,R)$, these equations may be written as

$$(U/J)_\tau + [(\xi_T U + \xi_X E + \xi_R F)/J]_\xi + [(\eta_T U + \eta_X E + \eta_R F)/J]_\eta + G = 0 \qquad (10)$$

where

$$U = \begin{bmatrix} \rho \\ \rho u \\ \rho v \\ \rho e_t \end{bmatrix} \quad E = \begin{bmatrix} \rho u \\ p+\rho u^2 \\ \rho uv \\ (\rho e_t + p)u \end{bmatrix} \quad F = \begin{bmatrix} \rho v \\ \rho uv \\ p+\rho v^2 \\ (\rho e_t + p)v \end{bmatrix} \quad G = \frac{1}{RJ} \begin{bmatrix} \rho v \\ \rho uv \\ \rho v^2 \\ (\rho e_t + p)v \end{bmatrix} \qquad (11)$$

and $J = \xi_X \eta_R - \xi_R \eta_X$ is the transformation Jacobian. In these equations, T denotes time, X the axial downstream coordinate, and R the cylindrical radial distance; u and v are the velocity components in the X and R directions; $e_t = p/[\rho(\gamma-1)] + (u^2 + v^2)/2$ and subscripts denote partial derivatives with respect to the indicated variable.

The analysis commences by introducing a computational mesh in polar (r,β) coordinates such that one family of coordinates consists of rays from the planetary center spaced at equal increments of β measured from the obstacle nose and the other of curved lines intersecting each ray so as to divide the portion of it between the magneto/ionopause and the shock wave into a fixed number of equal segments. The coordinate transformation equation is then used to map the portion of the X,R,T physical space bounded by (1) the bow wave, (2) the downstream outflow boundary at $\beta = \pi/2$, (3) the obstacle surface, and (4) the stagnation streamline at $\beta = 0$ into a rectangle in the ξ, η, τ computational space as illustrated in Figure 1. Generally, the transformation metrics at each time step are not known beforehand and must be determined numerically as part of the solution. Integration step size is established by using the eigenvalues of the Jacobian matrices $\bar{A}$ and $\bar{B}$, where $\bar{A} = \partial\hat{E}/\partial\hat{U}$, $\bar{B} = \partial\hat{F}/\partial\hat{U}$, and also where $\hat{U} = U/J$, $\hat{E} = (\xi_T U + \xi_X E + \xi_R F/J$, and $\hat{F} = (\eta_T U + \eta_X E + \eta_R F)/J$.

Boundary conditions for a properly posed mathematical problem are that the flow satisfy the axisymmetric Rankine-Hugoniot shock relations derivable from equation (10) along item 1 above, be entirely supersonic along item 2 above, be parallel to items 3 and 4 above, and be symmetric about item 4 above. Initial conditions are determined by use of an approximating formula for the coordinates of the bow shock wave, dependent on γ, M_∞, and the shape of the obstacle, and by prescribing a Newtonian pressure distribution on the obstacle. The remainder of the initial properties on the obstacle surface can then be determined from the conditions that the flow must be tangential to the surface and possess constant entropy. A linear variation for the flow properties between the bow shock and the obstacle is then prescribed. This provides the initial flow field, which is then integrated in a time asymptotic fashion until the steady state solution is obtained.

The basic numerical algorithm used in the IMP code was developed by Beam and Warming [1976] and is second-order accurate, noniterative and

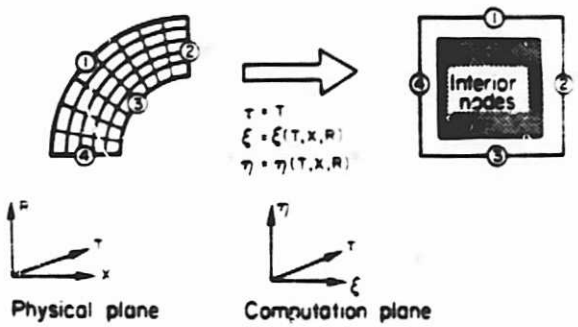

Fig. 1. Transformation from physical domain to rectangular domain.

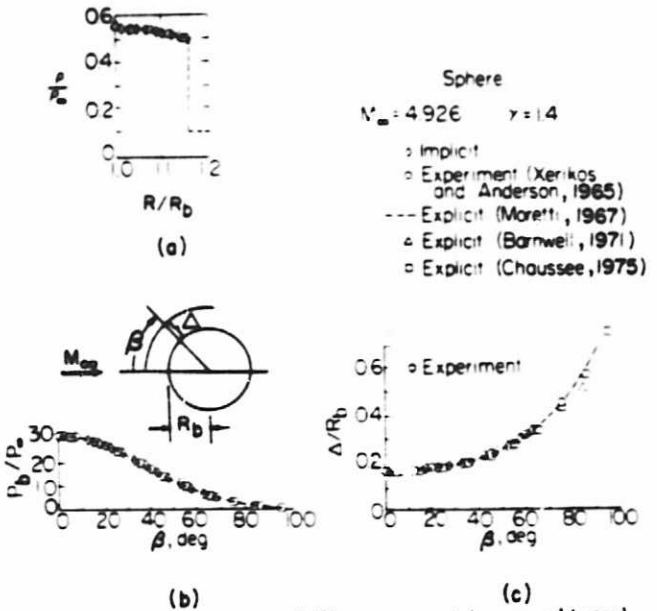

Fig. 2. Comparison of flow properties predicted by present implicit method with other techniques and experiment for supersonic flow past a sphere; $M_\infty = 4.926$, $\gamma = 1.4$. (a) Stagnation line density. (b) Surface pressure. (c) Shock standoff distance.

spatially factored. In particular, the 'delta form' with Euler time differencing is employed. When applied to (10), the algorithm assumes the form

$$(I + \Delta\tau\delta_\xi \bar{A}^n)(I + \Delta\tau\delta_\eta \bar{B}^n)(\hat{U}^{n+1} - \hat{U}^n) = -\Delta\tau(\delta_\xi \hat{E}^n + \delta_\eta \hat{F}^n + G) \qquad (12)$$

where $\bar{A}$ and $\bar{B}$ are the Jacobian matrices, I is the identity matrix, δ_ξ and δ_η are second-order, central difference operators, $\hat{U}^{n+1} = \hat{U}(n\Delta\tau)$, and $\Delta\tau$ is the integration step size.

Equation (12) is solved at the interior points only. It requires two 4x4 block tridiagonal inversions at each time step of the integration. The solution proceeds as follows:

1. Define $\Delta\hat{U} = \hat{U}^{n+1} - \hat{U}^n$.
2. Form the right-hand side of (12), and store results in the $\hat{U}^{n+1}$ array.
3. Apply smoothing $\hat{U}^{n+1} = \hat{U}^{n+1} - (\epsilon/8)S/J$.
4. Define $\bar{U} = (I + \Delta\tau\delta_\eta \bar{B}^n)\Delta\hat{U}$, and solve the matrix equation $(I + \Delta\tau\delta_\xi \bar{A}^n)\bar{U} = \hat{U}^{n+1}$ for $\bar{U}$, storing the result in the $\hat{U}^{n+1}$ array.
5. Solve the matrix equation $(I + \Delta\tau\delta_\eta \bar{B}^n)\Delta\hat{U} = \hat{U}^{n+1}$ for $\Delta\hat{U}$.
6. Obtain the values of $\hat{U}^{n+1}$ from the relation $\hat{U}^{n+1} = \Delta\hat{U} + \hat{U}^n$.
7. Transfer the contents of $\hat{U}^{n+1}$ to $\hat{U}^n$, and repeat all steps until satisfactory convergence is attained.

S is a fourth-order smoothing term introduced to eliminate nonlinear stabilities that may arise, since the use of central differences in the spatial directions results in a neutrally stable algorithm.

At the boundaries, modification of the differencing algorithm to account for the particular conditions described above is accomplished as follows. The obstacle surface flow tangency condition is incorporated through the use of Kentzer's [1970] scheme, while at the symmetry plane the variables are reflected according to whether they are odd or even. At the outflow boundary, where the flow is entirely supersonic, the dependent variables are determined by extrapolation from the adjacent interior points. For the upstream boundary, formed by the bow shock wave, the sharp discontinuity approach of Thomas et al. [1972] is used. The interior flow field bounded by these various boundaries is treated in shock-capturing fashion and therefore allows for the correct formation of secondary internal shocks should any occur.

Shock-Capturing Marching Solution for the Downstream Solution

The shock-capturing technique of Kutler et al. [1973] and Chaussee et al. [1975] employed herein is based on the set of four equations for steady axisymmetric flow obtained from (10) and (11) by

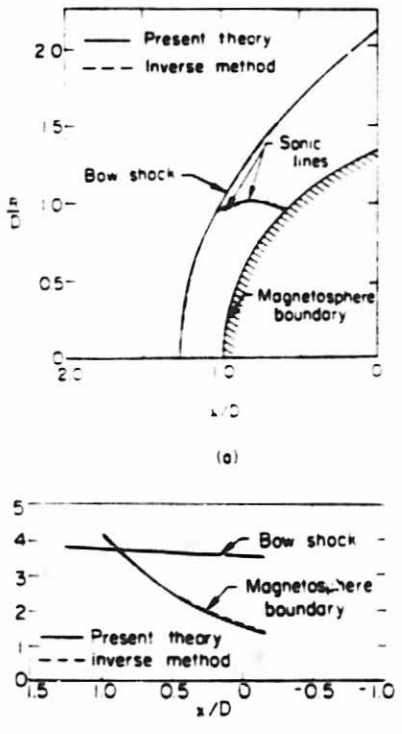

Fig. 3. Comparison of implicit and inverse methods for shock shape and sonic line location and density distribution along bow shock and magnetosphere boundary for $M_\infty = 8$, $\gamma = 5/3$ flow past the rotated equatorial trace of the magnetopause. (a) Shock shape and sonic line location. (b) Density distribution.

setting the τ derivatives to zero. The fourth of this set of equations, which represents conservation of total energy ρe_t, can be integrated to obtain the relation $h_t = e_t + p/\rho$ = const for the total enthalpy per unit mass.

The computational mesh is defined by lines of constant X and $(r-r_b)/(R_s-R_b)$, where R_b and R_s are functions of X that describe the radial cylindrical coordinates of the magneto/ionopause and bow shock wave at the same X as the field point (X,R) illustrated in Figure 1. The three remaining partial differential equations for conservation of mass and of axial and radial momentum are then transformed to a rectangular computational space by $\xi = X$, $\eta = (R-R_b)/(R-R_b)$ to obtain

$$\frac{\partial \tilde{E}}{\partial \xi} + \frac{\partial \tilde{F}}{\partial \eta} + \tilde{G} = 0 \qquad (13)$$

where

$$\tilde{E} = E$$

$$\tilde{F} = \{F - [\frac{\partial}{\partial \xi} R_b + \eta \frac{\partial}{\partial \xi} (R_s - R_b)]\}/(R_s - R_b)$$

$$\tilde{G} = G + \frac{E}{R_s - R_b} \frac{\partial}{\partial \xi} (R_s - R_b) \qquad (14)$$

The finite difference counterpart of (13) is integrated with respect to the hyperbolic coordinate ξ to yield values for the conservative variable E. Subsequent to each integration step the physical flow variables p, ρ, u, and v must be decoded from the components e_i of E. This necessitates the solution of four simultaneous, nonlinear equations and is facilitated by using the relations $v = e_3/e_1$, $p = e_2 - e_1 u$, $\rho = e_1/u$,

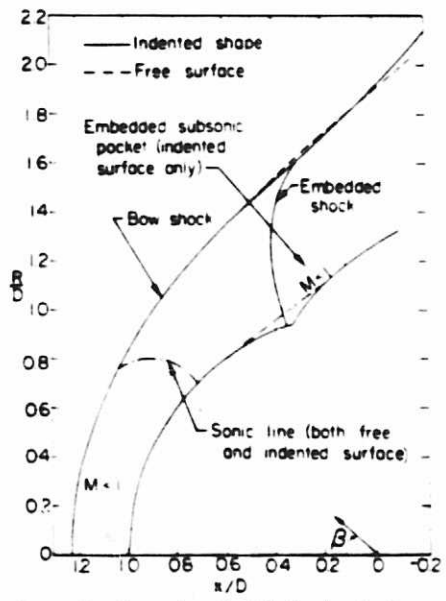

Fig. 4. Bow shock and embedded shock locations for solar wind flow with $M_\infty = 5$, $\gamma = 5/3$ past the rotated principal meridian of the magnetopause.

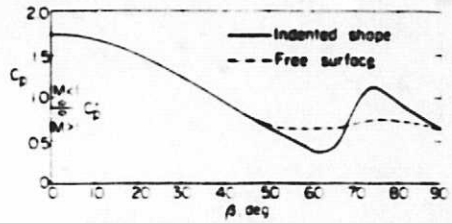

Fig. 5. Magnetopause pressure coefficients for the principal meridian magnetopause shapes shown in Figure 4.

and $h = \gamma/(\gamma-1)(p/\rho)$ to determine the following quadratic equation for u:

$$\frac{u^2}{2} + \frac{\gamma}{\gamma-1}\left(\frac{e_2 - e_1 u}{e_1}\right)u - h_t + \left(\frac{e_3}{e_1}\right)^2$$

$$= -\frac{\gamma+1}{2(\gamma-1)}u^2 + \left(\frac{\gamma}{\gamma-1}\right)\frac{e_2}{e_1}u - h_t + \left(\frac{e_3}{e_1}\right)^2 = 0 \qquad (15)$$

Two roots exist; one corresponds to subsonic flow and is discarded, since u is always supersonic in the present application, while the other corre-

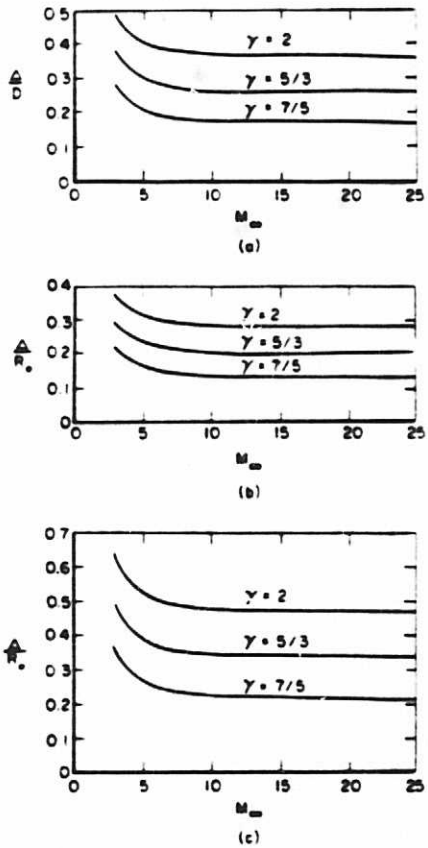

Fig. 6. Variation of shock standoff distance with oncoming Mach number and ratio of specific heats for various magneto/ionopause traces as determined by the present implicit procedure. (a) Magnetopause equatorial trace. (b) Ionopause trace $-H/R_0 = 0.01$. (c) Ionopause trace $-H/R_0 = 0.5$.

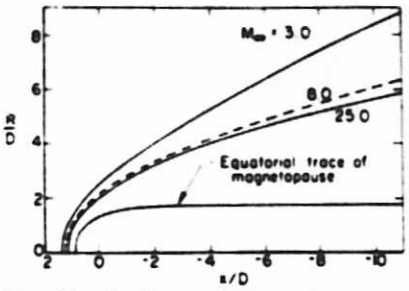

Fig. 7. Shock shapes for various supersonic flows past the rotated equatorial trace of the magnetopause; combined near (blunt body) and far (marching) solutions.

sponds to supersonic flow and gives the desired solution.

Since only the bow shock wave is treated as a sharp discontinuity and any others that may be present are 'captured' by the difference algorithm selection of the appropriate finite difference scheme to advance the calculation in the ξ direction is of prime importance. As in the blunt body aerodynamic analysis of Kutler et al. [1973] and Chaussee et al. [1975], the numerical integration of (13) is accomplised by using the finite difference predictor-corrector scheme of MacCormack [1969] the most efficient second-order algorithm for shock-capturing calculations.

Calculation of the Streamlines

The streamlines are determined by integrating trajectories through the known velocity field, as this procedure was found to be more accurate than the alternative mass flow calculation. The calculation of a particular streamline is initiated at the bow shock, where its slope is calculated with an exact gasdynamic relation contained implicitly in both the blunt body (IMP) and marching (SCT) solution, and continued by stepwise integration in X using a modified third-order Euler predictor-corrector method. Bivariate linear interpolation from the flow field grid points is employed to obtain the velocity components (u,v) required at the stepwise points along the streamline trajectory.

Calculation of the Magnetic Field

With the flow properties known from the gasdynamic solution, calculation of the magnetic field $\underline{B}$ proceeds by integrating the steady state counterpart of (4), commonly interpreted as indicating that the field lines move with the fluid. This leads to a straightforward calculation in which the vector distance from each point on an arbitrarily selected field line to its corresponding point on an adjacent field line in the downstream direction is determined by numerically integrating $\int \underline{V}\, dt$ over a fixed time interval δt. Once the coordinates of the field lines are determined, the magnetic field at any point may be calculated from the relation $\underline{B}/|\underline{B}_\infty| = \rho \Delta \underline{\ell} / (\rho_\infty |\Delta \underline{\ell}_\infty|)$, where $\Delta \underline{\ell}$ is the vector length of a small element of a flux tube.

Such a procedure is valid generally, but its use in the present calculations is confined to only one component of the magnetic field. The other components are determined by use of the Alksne and Webster [1970] decomposition dependent upon the axisymmetric properties of the gasdynamic solution and the linearity of the magnetic equations.

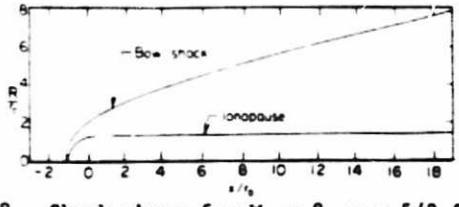

Fig. 8. Shock shape for $M_\infty = 8$, $\gamma = 5/3$ flow past an ionopause shape with $H/R_0 = 0.1$: combined near (blunt body) and far (marching) field solutions.

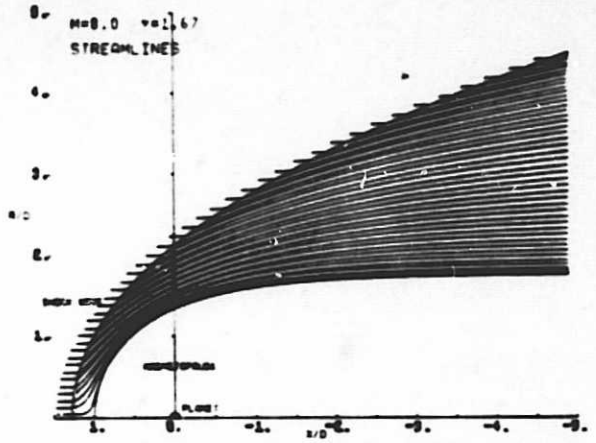

Fig. 9a. Streamline map for $M_\infty = 8.0$, $\gamma = 5/3$ flow past the rotated equatorial trace of the magnetopause: combined blunt body and marching flow field.

Calculation of the Contour Lines

Contours are calculated for nondimensionalized velocity $|\underline{V}|/V_\infty$, density ρ/ρ_∞, and magnetic field

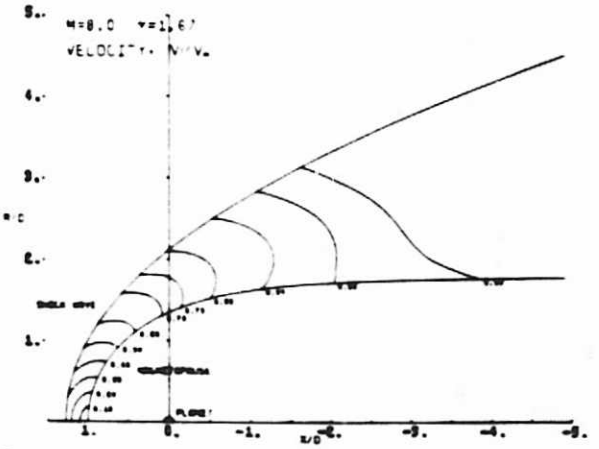

Fig. 9b. Velocity map for $M_\infty = 8.0$, $\gamma = 5/3$ flow past the rotated equatorial trace of the magnetopause: combined blunt body and marching flow field.

components $(B/B_\infty)_\parallel$ and $(B/B_\infty)_\perp$ by application of a searching procedure. After a value for the contour line is specified, the shock boundary is searched for intervals which bracket the selected value. After one such point is located by interpolation, the remainder of the contour is determined by 'walking' around the contour, searching each step for the interval and then interpolating to find the point through which the contour passes. This is repeated until a boundary point is reached. The closed contours are found in a similar manner. Linear interpolation is used throughout the process. The coordinates of the contour lines are output as listings, pen plots, or both.

Results and Discussion

To verify the correctness of the new procedures and to demonstrate their capability for calculating solar wind flows for a variety of conditions, a large number of test cases have been run, and a sample have been evaluated by comparison with previously available theoretical and experimental results. Figure 2 presents such a comparison for supersonic flow of air (γ=1.4) past a sphere at M_∞ = 4.926. The variation of density along the stagnation streamline is provided in Figure 2a, while the variations of surface pressure p_b and shock standoff distance Δ with angular distance from the nose are given in Figures 2b and 2c. In these and similar comparisons the results provided by the new procedures are in essentially perfect agreement with those of previous numerical solutions and experiment.

Figure 3 exhibits a comparison of results predicted by the present method with those originally calculated by Spreiter et al. [1966, 1968] for the same solar wind and magnetosphere conditions, using the inverse method of Inouye and Lomax [1962] for the blunt nose region and the method of characteristics for the downstream supersonic region. Figure 3a displays the locations of the bow wave and sonic line for flow past the equatorial trace of the magnetopause for M_∞ = 8 and γ = 5/3. The density distribution along the magnetosphere boundary and along the shock wave are given in Figure 3b. Essentially perfect agreement is obtained between the present implicit technique and the inverse method. Similarly perfect agreement has been obtained with all of the results presented previously in the cited references by Spreiter and his colleagues. The present method is, however, both more efficient and more versatile.

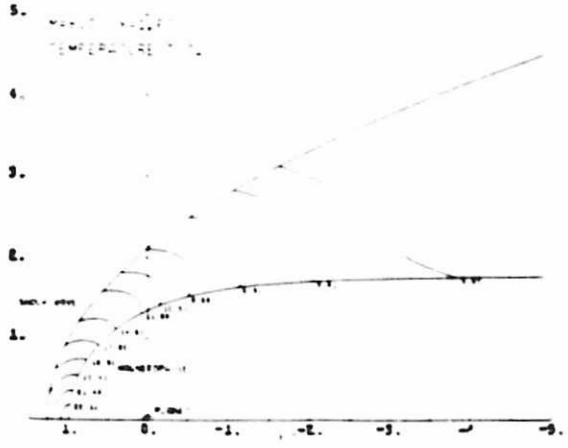

Fig. 9c. Temperature map for M_∞ = 8.0, γ = 5/3 flow past the rotated equatorial trace of the magnetopause: combined blunt body and marching flow field.

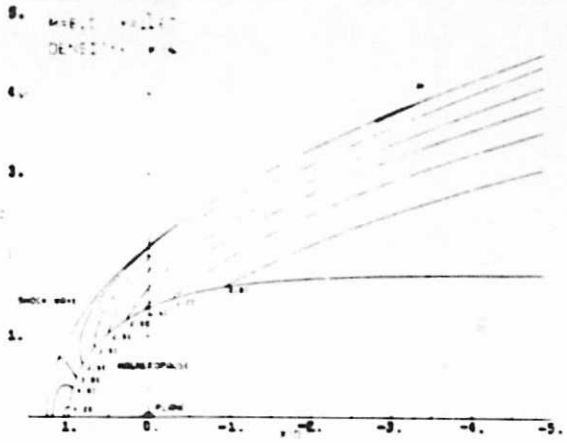

Fig. 9d. Density map for M_∞ = 8.0, γ = 5/3 flow past the rotated equatorial trace of the magnetopause: combined blunt body and marching flow field.

Figures 4 and 5 present new results that illustrate the geometric flexibility of the present solution and its ability to capture embedded shock waves as well as the bow shock, a feature which the inverse method cannot duplicate. This case is for M_∞ = 5 and γ = 5/3 flow around the axisymmetric shape generated by rotating the principal meridian of an indented magnetopause about its axis and may be compared with an experimental test by Spreiter et al. [1968]. This particular profile shape, derived by Spreiter and Briggs [1962] from the Beard [1960] approximation to the classical Chapman and Ferraro [1931] theory, contains a pronounced dent with a concave corner in the vicinity of a magnetic neutral point. Spreiter and Summers [1967] argued that the presence of an embedded shock wave would make it impossible for the magnetosheath plasma to follow such an indented contour and that there would form instead a free surface approximating, in the meridian plane, a tangent line across the indentation and capping an embedded cusp region. Figure 4 presents results for both the indented and the free surfaces, denoted by solid and dashed lines. For the indented surface a shock wave is located on the body at approximately θ = 80°, just as in the experiment, while for the free surface the pressure coefficient displays an approximately constant value as anticipated. Finally, we note that the calculation of a supersonic flow with an embedded shock and subsequent subsonic pocket provides a severe test for any blunt body procedure. The ability of the present code to provide convergent results for such a flow demonstrates the capability for further extension and application to more generalized profiles than was heretofore possible.

As a final illustration of the range of conditions for which the implicit code has been tested, Figure 6 summarizes results for the shock standoff

distance provided by the gasdynamic calculations for three values for γ for three different magneto/ionopause shapes and a range of values for M_∞ from 3 to 25. These conditions span the range of interest of geometrical and solar wind conditions for which the computer programs developed herein would be normally applied.

In order to confirm the ability of the marching code to continue the solution to some arbitrarily specified downstream location, solutions have been carried far downstream for a wide variety of cases typical of solar wind interactions. Figure 7 exhibits the location of the bow wave downstream from the nose region to $x/D = -11$ for flows with $\gamma = 5/3$ and $M_\infty = 3$, 8, and 25 past the rotated equatorial trace of the magnetopause. For this calculation, starting conditions for the marching code (SCT) are provided by the blunt body (IMP) code on the line $x/D = 0.0$, which is the usual location at which the two solutions are joined by the computer program. The marching code then determines the remainder of the flow field back to the specified downstream location. Since for the shapes considered herein the downstream flows are quite smooth, the marching calculation is very efficient (less than 30s, CDC 7600, OPT=2 compiler). Similar results are presented in Figure 8 for $M_\infty = 8$ and $\gamma = 5/3$ flow past an ionopause shape with $H/R_0 = 0.1$. Those results have been carried to $x/R_0 = -20$ in keeping with the observation that R_0 for Venus and Mars is only slightly greater than the planetary radius, whereas for the earth, D is of the order of 10 earth radii.

To illustrate the capability of the present procedures to determine streamlines, contour maps of various flow properties, and magnetic field lines and contours, as well as to demonstrate the automated plotting capability for displaying these results, Figures 9 and 10 have been prepared. Figure 9 illustrates the computer-generated streamline locations and contour maps of velocity ratio V/V_∞, temperature ratio T/T_∞, and density ratio ρ/ρ_∞ for the complete near- and far-field flow about the equatorial trace of the magnetosphere for $M_\infty = 8$ and $\gamma = 5/3$. Based on this gasdynamic solution, Figure 10 exhibits the corresponding results for the magnetic field $(B/B_\infty)_\perp$ and $(B/B_\infty)_\parallel$ in the plane of magnetic symmetry for B_∞ parallel and perpendicular to V_∞. In addition to demonstrating the overall smoothness of the computed results these two figures illustrate the ability of the present techniques to provide the completely automated production of report quality plots of both gasdynamic and magnetic field properties for solar wind flows past axisymmetric magneto-ionopause shapes.

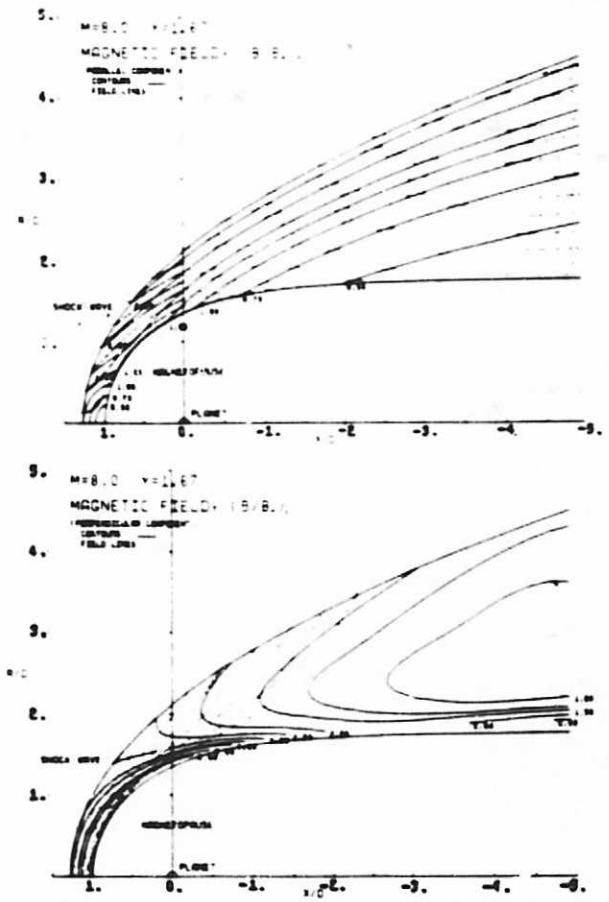

Fig. 10. Contours and field line locations of the magnetic field components $(B/B_\infty)_\perp$ and $(B/B_\infty)_\parallel$ in the plane of magnetic symmetry for $M_\infty = 8.0$ and $\gamma = 5/3$ flow past the rotated equatorial trace of the magnetopause.

Concluding Remarks

Advanced numerical techniques have been applied to produce an efficient operational computer solution for the well-established dissipationless magnetogasdynamic model for axisymmetric, supersonic, super-Alfvénic solar wind flow past either magnetic or nonmagnetic terrestrial planets. The solution consists of the following assemblage of computer codes; (1) blunt body code, to determine the gasdynamic solution near the magneto/ionopause nose, (2) marching code, to determine the gasdynamic solution downstream of the magneto/ionopause nose, (3) streamline code, to determine coordinates of flow field streamlines, (4) magnetic field code, to determine frozen-in magnetic field, (5) contour code, to determine coordinates of contour lines of flow and magnetic field properties, and (6) plotting code, to plot selected flow and magnetic field results.

Comparisons are reported which demonstrate the accuracy of the present techniques by comparison with previously established theoretical methods and with experimental data. New results are presented for a variety of solar wind flows which illustrate the flexibility and generality of the methods.

Acknowledgments. This work was supported by the National Aeronautics and Space Administration under contracts NASW-2945 and NASW-3184 with I. Schmerling and R. Murphy as technical monitors.

References

Alksne, A. Y., The steady-state magnetic field in the transition region between the magnetosphere and the bow shock, Planet. Space Sci., 15, 239, 1967.

Alksne, A. Y., and D. L. Webster, Magnetic and

electric fields in the magnetosheath, Planet. Space Sci., 18, 1203, 1970.

Barnwell, R. W., A time-dependent method for calculating supersonic angle-of-attack flow about axisymmetric blunt bodies with sharp shoulders and smooth nonaxisymmetric blunt bodies, NASA Tech. Note, TN D-6283, 1971.

Beam, R. M., and R. F. Warming, An implicit finite-difference algorithm for hyperbolic systems in conservation-law form, J. Comput. Phys., 22, 1, 1976.

Beard, D. B., The interaction of the terrestrial magnetic field with the solar corpuscular radiation, J. Geophys. Res., 65, 3559, 1960

Chapman, S., and V. C. A. Ferraro, An outline of a theory of magnetic storms, J. Geophysics Res., 36, 77, 171, 1931.

Chaussee, D. S., T. Holtz, and P. Kutler, Inviscid supersonic/hypersonic body flow fields and aerodynamics from shock-capturing technique calculations, AIAA Pap. 75-837, 1975.

Crooker, N. U., and G. L. Siscoe, A mechanism for pressure anisotropy and mirror instability in the dayside magnetosheath, J. Geophys. Res., 82, 185, 1977.

Dryer, M., and R. Faye-Petersen, Some observations from an approximate solution of the direct blunted body problem in hypersonic flow, Proceedings of the 1964 Heat and Transfer and Fluid Mechanics Institute, edited by W. H. Giedt and S. Levy, p. 160, Stanford University Press, Stanford, Calif., 1964.

Dryer, M., and R. Faye-Petersen, Magnetogasdynamic boundary condition for a self-consistent solution to the closed magnetopause, AIAA J., 4, 246, 1966.

Dryer, M., and G. R. Heckman, Application of the hypersonic analogy to the standing shock of Mars, Sol. Phys., 2, 112, 1967.

Inouye, M., and H. Lomax, Comparison of experimental and numerical results for the flow of a perfect gas about blunt-nosed bodies, NASA Tech. Doc., TD-1426, 1962.

Kentzer, C. P., Discretization of boundary conditions on moving discontinuities, Lect. Notes Phys., 8, 108-113, 1970.

Kutler, P., W. A. Reinhardt, and R. F. Warming, Multi-shocked, three-dimensional supersonic flow fields with real gas effects, AIAA J., 11, 657, 1973.

MacCormack, R. W., The effect of viscosity in hypervelocity impact cratering, AIAA Pap., 69-354, 1969.

Moretti, G. and G. Bleich, Three dimensional flow around blunt bodies, AIAA J., 5, 1557, 1967.

Spreiter, J. R., Magnetohydrodynamic and gasdynamic aspects of solar-wind flow around terrestrial planets: A critical review, NASA Spec. Publ., SP 397, 1976.

Spreiter, J. R., and A. Y. Alksne, Plasma flow around the magnetosphere, Rev. Geophys., 7, 11, 1969.

Spreiter, J. R., and A. Y. Alksne, Solar wind flow past objects in the solar system, Annu. Rev. Fluid Mech., 2, 1970.

Spreiter, J. R., and B. R. Briggs, Theoretical determination of the form of the boundary of the solar corpuscular stream produced by interaction with the magnetic dipole field of the earth, J. Geophys. Res., 67, 37, 1962.

Spreiter, J. R., and W. P. Jones, On the effect of a weak interplanetary magnetic field on the interaction between the solar wind and the geomagnetic field, J. Geophys. Res., 68, 3555, 1963.

Spreiter, J. R., and A. W. Rizzi, Aligned magnetohydrodynamics solution for solar wind flow past the earth's magnetosphere, Acta Astronaut., 1, 15, 1974.

Spreiter, J. R., and A. L. Summers, On conditions near the neutral points on the magnetosphere boundary, Planet Space Sci., 15, 787, 1967.

Spreiter, J. R., A. Y. Alksne, and A. L. Summers, External aerodynamics of the magnetosphere, in Physics of the Magnetosphere, edited by R. L. Carovillano, J. F. McClay, and H. R. Radoski, p. 301, D. Reidel, Hingham, Mass., 1968 (also available as NASA Tech. Note TN 4482, 1968).

Spreiter, J. R., A. L. Summers, and A. Y. Alksne, Hydromagnetic flow around the magnetosphere, Planet. Space Sci., 14, 223, 1966.

Spreiter, J. R., A. L. Summers, and A. W. Rizzi, Solar wind flow past nonmagnetic planets - Venus and Mars, Planet. Space Sci., 18, 1281, 1970.

Stahara, S. S., D. S. Chaussee, B. C. Trudinger, and J. R. Spreiter, Computational techniques for solar wind flows past terrestrial planets - Theory and computer programs, NASA Contract. Rep., CR 2924, 1977.

Thomas, P. D., M. Vinokur, R. Bastionon, and R. J. Conti, Numerical solution for the three-dimensional hypersonic flow field of a blunt delta body, AIAA J., 10, 887, 1972.

Zwan, B. J., and R. A. Wolf, Depletion of solar wind plasma near a planetary boundary, J. Geophys. Res., 81, 1636, 1976.

Xerikos, J., and W. A. Anderson, An experimental investigation of the shock layer surrounding a sphere in supersonic flow, AIAA J., 3, 451, 1965.

(Received January 26, 1980;
revised May 22, 1980;
accepted July 25, 1980.)

JOURNAL OF GEOPHYSICAL RESEARCH, VOL. 85, NO. A13, PAGES 7715-7738, DECEMBER 30, 1980

SOLAR WIND FLOW PAST VENUS: THEORY AND COMPARISONS

John R. Spreiter

Division of Applied Mechanics, Stanford University, Stanford, California 94305

Stephen S. Stahara

Nielsen Engineering & Research, Inc., Mountain View, California 94043

Abstract. Advanced computational procedures are applied to an improved model of solar wind flow past Venus to calculate the locations of the ionopause and bow wave and the properties of the flowing ionosheath plasma in the intervening region. The theoretical method is based on a single-fluid, steady, dissipationless, magnetohydrodynamic continuum model and is appropriate for the calculation of axisymmetric supersonic, super-Alfvénic solar wind flow past a nonmagnetic planet possessing a sufficiently dense ionosphere to stand off the flowing plasma above the subsolar point and elsewhere. Determination of time histories of plasma and magnetic field properties along an arbitrary spacecraft trajectory and provision for an arbitrary oncoming direction of the interplanetary solar wind have been incorporated in the model. An outline is provided of the underlying theory and computational procedures, and sample comparisons of the results are presented with observations from the Pioneer Venus orbiter.

Introduction

The magnetohydrodynamic model of Spreiter et al. [1970] for solar wind flow around the Venus ionosphere, stemming from the closely related earlier studies for the earth and its magnetosphere [Spreiter, 1976; Spreiter and Jones, 1963; Spreiter and Rizzi, 1974; Spreiter et al., 1966, 1968, 1970; Dryer and Faye-Peterson, 1966; Dryer and Heckman, 1967], provides a theoretical basis for the understanding and interpretation of observations from the viewpoint of a fluid rather than a particle description of the flow. The basic pattern for the associated calculations using this model was established by Spreiter et al. [1966] for the case of the earth, or any other planet with a dominant dipole magnetic field; and by Spreiter et al. [1970] for the case of Venus and Mars, or any other planet with no significant magnetic field but a sufficiently dense ionosphere to stand off the solar wind above the planetary surface. This consists of (1) representing the magnetopause or ionopause by a magnetohydrodynamic tangential discontinuity, (2) solving for the shape of the magnetospheric or ionospheric obstacle using simplified approximations for the pressure of the deflected solar wind flow at the obstacle boundary and for the planetary magnetic and atmospheric properties, (3) solving for the location of the bow wave and for the density, velocity, pressure, and temperature throughout the flow as a gasdynamic problem, disregarding the electromagnetic forces because of the characteristically high values of the free-stream Alfvén Mach number, and finally (4) calculating the magnetic field as a frozen-in convected field assuming that the other fluid properties are provided sufficiently accurately by the gasdynamic solution.

Prior to the work reported recently by Stahara et al. [1977], the utility of this model was severely restricted because results were available only in the form of plots in archival journals for a limited set of solar wind and planetary conditions. Results for intermediate points or for other conditions had to be determined by interpolation. Stahara et al. [1977] improved on the basic model in many significant ways. New and more effective algorithms were introduced to perform the calculations, enabling the determination of results for a wide range of specific conditions typical of solar wind/terrestrial planet interactions for both magnetic and nonmagnetic planets.

In the current work summarized here, that model has been extended and generalized in several important directions. These include (1) extension of the gasdynamic capability for treating free-stream Mach numbers as low as $M_\infty = 2$, (2) development of a new family of ionopause shapes which includes the effect of gravitational variation in scale height of the ionosphere, and (3) development of the capability for readily determining the plasma properties along an arbitrary spacecraft trajectory, simultaneously accounting for an arbitrary direction for the incident solar wind relative to a chosen coordinate system.

The Mathematical Model - Formulation of the Fluid Representation

The fundamental assumption underlying the present work and that reported in all of the references cited above is that many properties of solar wind flow around a planetary magneto/ionosphere can be adequately described by the continuum equations of magnetohydrodynamics for a single-component perfect gas having infinite electrical conductivity and zero viscosity and thermal conductivity.

Governing Equations

The magnetohydrodynamic equations for the conservation of mass, momentum, energy, and magnetic field are as follows:

$$\frac{\partial \rho}{\partial t} + \frac{\partial}{\partial x_k}(\rho v_k) = 0 \qquad (1)$$

$$\frac{\partial}{\partial t}(\rho v_i) + \frac{\partial}{\partial x_k}\left[\rho v_i v_k + p\delta_{ik} - \frac{B_i B_k}{4\pi}\right.$$

Paper number 80A0479.
0148-0227/80/080A-0479$01.00

$$+ \frac{B^2}{8\pi}\delta_{ik} + \frac{g_i g_k}{4\pi G} - \frac{g^2}{8\pi G}\delta_{ik}\Big] = 0 \qquad (2)$$

$$\frac{\partial}{\partial t}\left(\frac{\rho v^2}{2} + \rho e + \rho\phi + \frac{B^2}{8\pi}\right)$$

$$+ \frac{\partial}{\partial x_k}\left[\rho v_k\left(\frac{v^2}{2} + e + \frac{p}{\rho} + \phi\right) + S_k\right] = 0 \qquad (3)$$

$$\frac{\partial B_i}{\partial t} = \frac{\partial}{\partial x_k}(v_i B_k - v_k B_i), \quad \frac{\partial B_i}{\partial x_i} = 0 \qquad (4)$$

where

$$g_i = -\frac{\partial\phi}{\partial x_i}, \quad S_k = \frac{1}{4\pi}\left(v_k B^2 - B_k v_i B_i\right) \qquad (5)$$

and the equation of state of a perfect gas is given by

$$p = \frac{\rho\bar{R}T}{\bar{M}} \qquad (6)$$

In these equations and those to follow, the symbols ρ, p, v, T, $e = C_v T$, and $h = C_p T$ refer to the density, pressure, velocity, temperature, internal energy, and enthalpy, and C_v and C_p refer to the specific heats at constant volume and pressure in the usual way. The symbol $\bar{R} = (C_p - C_v)\bar{M} = 8.3\times10^7$ erg/g°K is the universal gas constant, and $\bar{M}$ is the mean molecular weight nondimensionalized so that $\bar{M} = 16$ for atomic oxygen. For fully ionized hydrogen, $\bar{M}$ is thus 1/2. The magnetic field $\underline{B}$ and the Poynting vector $\underline{S}$ for the flux of electromagnetic energy are expressed in terms of Gaussian units. The gravitational potential ϕ and acceleration of gravity g are assumed to be due to massive fixed bodies so that their time derivatives are zero. $G = 6.67\times10^{-8}$ cm^3/g s^2 is the gravitational constant. These equations apply in the region exterior to the ionosphere boundary, as shown in Figure 1, and also in a degenerate sense in the ionosphere.

Because of the omission of dissipative terms in these equations, surfaces of discontinuity may develop in the solution, across which the fluid magnetic properties change abruptly, but in such a way that mass momentum, energy, and magnetic flux are conserved. These are approximations to comparatively thin surfaces across which similar but continuous changes in the fluid and magnetic properties occur in the corresponding theory of a dissipative gas, and they correspond physically to the bow wave, ionosphere boundary, and possibly other thin regions of rapidly changing properties. The conservation of mass, momentum, energy, and magnetic flux lead to the following relations between the quantities on the two sides of any such discontinuity:

$$[\rho v_n^*] = 0 \qquad (7)$$

$$[\rho\underline{v}\cdot v_n^* + (p + B^2/8\pi)\hat{n} - B_n\underline{B}_t/4\pi] = 0 \qquad (8)$$

$$\left[v_n^*\left(\frac{1}{2}\rho v^2 + \rho e + p + \frac{B^2}{4\pi}\right)\right.$$

$$\left. + q_n\cdot\left(p + \frac{B^2}{8\pi}\right) - \frac{B_n(\underline{v}\cdot\underline{B})}{4\pi}\right] = 0 \qquad (9)$$

$$[\underline{B}_t\cdot v_n^* - B_n\cdot\underline{v}_t] = 0 \qquad (10)$$

Here, (n, t) denote unit vectors normal and tangential to the discontinuity surface, where q_n represents the local normal velocity of the discontinuity surface and $v_n^* = v_n - q_n$ is the fluid normal velocity component relative to the normal velocity q_n of the discontinuity surface. The square brackets are used to indicate the difference between the enclosed quantities on the two sides of the discontinuity, as in $[Q] = Q_2 - Q_1$, where subscripts 1 and 2 refer to the conditions on the upstream and downstream sides, respectively, of the discontinuity. Correspondingly, the average of Q_1 and Q_2 is represented by $\langle Q\rangle = (Q_1 + Q_2)/2$.

Five classes of discontinuities are described by (7)-(10). Of these, only two, the fast shock wave and the tangential discontinuity, are of significance in the present analysis. The former, having properties that satisfy the relations

$$v_n^* \neq 0 \quad [\rho] > 0 \quad [p] > 0 \quad [B_n] = 0$$

$$[\underline{B}_t] > 0 \quad [B^2] > 0 \quad (\rho v_n^*)^2 > B_n^2/(4\pi\langle 1/\rho\rangle) \qquad (11)$$

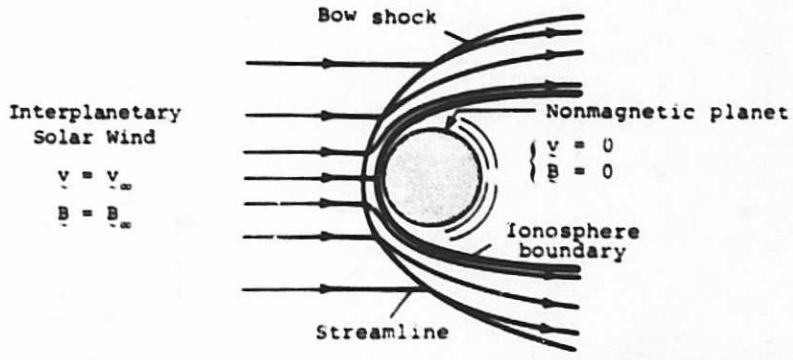

Fig. 1. Illustration of overall features of solar wind interaction with nonmagnetic terrestrial planets.

is appropriate for representing the bow wave; and the latter, having properties given by

$$v_n^* = B_n = 0 \qquad [v_t] \neq 0 \qquad [B_t] \neq 0$$
$$[\rho] \neq 0 \qquad [p + B^2/8\pi] = 0 \tag{12}$$

is appropriate for representing the ionopause that separates the flowing solar wind and the planetary ionosphere.

High Alfvén Mach Number Approximation

Two important parameters that characterize steady magnetohydrodynamic flow past a stationary obstacle are the free-stream Mach number $M_\infty = v_\infty/a_\infty$ and the Alfvén Mach number $M_{A_\infty} = v_\infty/A_\infty$, in which $a = (\gamma p/\rho)^{1/2}$ is the speed of sound and $A = (B^2/4\pi\rho)^{1/2}$ is the speed of a rotational or Alfvén wave along the direction of the magnetic field, and $\gamma = C_p/C_v$ is the ratio of specific heats of the plasma.

For typical solar wind conditions at Venus, both M_∞ and M_{A_∞} are high, values of the order of 10 being representative. As a result, important simplifications of the equations may be introduced. Since the order of magnitude of the momentum flux term in (2) and the kinetic energy flux term in (3) is related to that of the magnetic terms in the same equations by the square of M_{A_∞}, consideration of the magnetic terms may be decoupled from the solution of the gasdynamic portions of those equations. The equations for the fluid motion thereby reduce approximately to those of gasdynamics, and the magnetic field $\underset{\sim}{B}$ can be determined subsequently by solving the remaining equations using the values for ρ and $\underset{\sim}{v}$ so determined. Furthermore, because of the large value for M_∞, the terms involving g and Φ can be disregarded in the solar wind flow because of the relatively small effects of gravity on the flow. This is not true, of course, in the ionosphere, where the comparative stationarity of the gases results in a very nearly hydrostatic variation of the pressure with altitude.

The precise specification of the range of usefulness of the decoupled approximation remains elusive in the absence of exact solutions of the complete magnetohydrodynamic equations. The only such solutions for the present category of flows are those of Spreiter and Rizzi [1974] for the special case in which $\underset{\sim}{B}_\infty$ is aligned with $\underset{\sim}{v}_\infty$. They indicate results virtually identical to those of the simpler decoupled theory when M_{A_∞} is about 10 or greater and notably differing results as M_{A_∞} is decreased below 5.

For other magnetic field alignments one can only make estimates of the relative magnitudes of the divergences of the neglected magnetic terms $B_iB_k/4\pi + B^2\delta_{ik}/8\pi$ and S_{ik} compared to the terms $\rho v_i v_k + p\delta_{ik}$ and $\rho v_k(v^2/2 + e + p/e)$ retained in the gasdynamic analysis and then speculate about how large the magnetic terms can become before they invalidate the solution. In regions where the momentum flux and kinetic energy terms are large in comparison with the pressure and enthalpy terms, the square of the local Alfvén Mach number $M_A^2 = (\rho v^2/2)\div(B^2/8\pi)$ may be considered to provide a rough measure of the dominance of the gasdynamic terms in the calculation of the fluid motion. Since this quantity is related to $M_{A_\infty}^2$ by $M_A = (\rho/\rho_\infty)(v/v_\infty)^2 \cdot (B_\infty/B)^2 M_{A_\infty}$, and ρ/ρ_∞, v/v_∞, and B/B_∞ are independent of M_{A_∞} at large M_{A_∞}, it follows that M_A tends to remain large for large M_{A_∞} except where $\rho v^2 \ll \rho_\infty v_\infty^2$ or where $B^2 \gg B_\infty^2$. These conditions are most likely to be encountered near the stagnation point, where v vanishes; but p reaches a maximum value comparable to $\rho_\infty v_\infty^2$ there, and that contravenes the initial premise upon which the estimate is predicated. A localized region of small M_A does not therefore necessarily signal a failure of the approximation.

As a further consideration in making such estimates, it should be noted that the orientation of $\underset{\sim}{B}_\infty$ is very important in the determination of B^2/B_∞^2 throughout the flow. In particular, near the stagnation point, $B^2/B_\infty^2 \gg 1$ if $\underset{\sim}{B}_\infty$ makes a substantial angle with $\underset{\sim}{v}_\infty$; whereas B^2/B_∞^2 vanishes at the stagnation point when $\underset{\sim}{B}_\infty$ is parallel to $\underset{\sim}{v}_\infty$, since $\underset{\sim}{B}$ is everywhere proportional to $\rho\underset{\sim}{v}$ [Spreiter and Rizzi, 1974]. For this case therefore $M_A^2 = (\rho_\infty/\rho)M_{A_\infty}^2$, and M_A does not vanish even at the stagnation point because ρ/ρ_∞ is about 4-5 for representative conditions.

A definitive theoretical evaluation of the decoupled approximation will have to await the development of more advanced methods for the solution of the complete magnetohydrodynamic equations. In the meanwhile, considerable insight can be gained by comparing the predictions with conditions actually measured in space during appropriately steady conditions. The small scale of the Venus flow field compared with that of the earth's magnetosphere makes the data from Pioneer Venus particularly valuable for this purpose; and the results presented here show our initial efforts to carry out such comparisons. This should be considered no more than a beginning, however, as we only have data from two orbits; many additional comparisons should be carried out to obtain a more comprehensive understanding of the relation between the theoretical and observational results.

Under the conditions outlined above, (2), (3), (8), and (9) are thus simplified to the following:

$$\frac{\partial}{\partial t}(\rho v_i) + \frac{\partial}{\partial x_k}(\rho v_i v_k + p\delta_{ik}) = 0 \tag{13}$$

$$\frac{\partial}{\partial t}\left(\frac{\rho v^2}{2} + \rho e\right) + \frac{\partial}{\partial x_k}\left[\rho v_k\left(\frac{v^2}{2} + e + p/\rho\right)\right] = 0 \tag{14}$$

$$[\rho\underset{\sim}{v} \cdot \underset{\sim}{v}_n^* + p] = 0 \tag{15}$$

$$\left[\underset{\sim}{v}_n^* \cdot \left(\frac{1}{2}\rho v^2 + \rho e + p\right)\right] = 0 \tag{16}$$

These equations, together with (1) and (7), are just those of gasdynamics and must be solved for the location of the bow wave and the gasdynamic properties $\underset{\sim}{v}$, p, ρ, and T of the flow field about the ionospheric obstacle. With these properties so determined, (4) and (10) can be used to determine the magnetic field B. Although all of the solutions described here are for the steady state

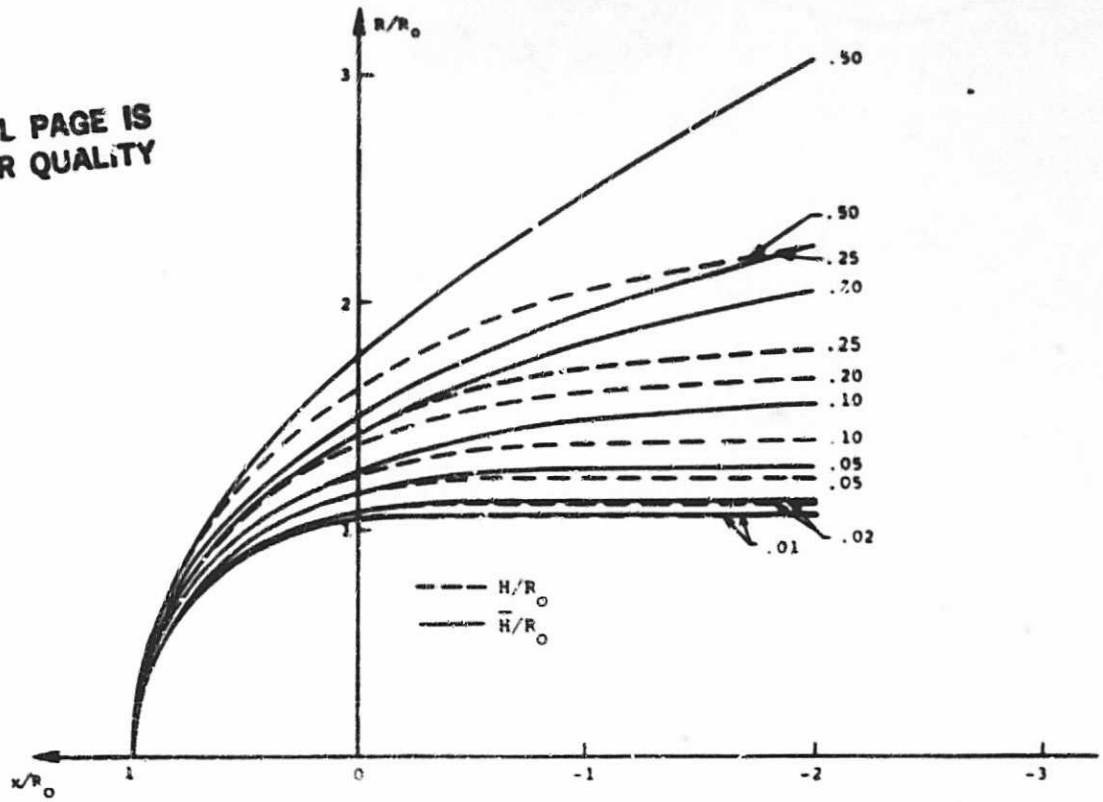

Fig. 2. Illustration of ionopause shapes for atmospheres with various (1) constant scale heights H/R_o and (2) gravitationally varying scale heights associated with a constant $T/\bar{M}$ atmosphere and characterized by $\bar{H}/R_o$.

obtained by setting $\partial/\partial t = 0$, and $v_n^* = v_n$, i.e., $q_n = 0$, the unsteady equations are presented in the foregoing because one of the computational methods used to determine the gasdynamic solution employs an unsteady procedure, integrating in time until the steady state solution is obtained asymptotically.

Determination of the Ionosphere Boundary

The determination of the ionosphere boundary, or ionopause, makes use of the idealization that the ionospheric plasma is spherically symmetric, hydrostatically supported, infinitely electrically conducting, devoid of any magnetic field, gravitationally bound to the planet, and incapable of mixing with the solar wind plasma, as sketched in Figure 1. This interior plasma is considered to be separated from the flowing solar wind plasma by a tangential discontinuity across which the relations of (12) apply. Because the magnetic pressure $B^2/8\pi$ is much smaller than the ionized gas pressure p in the ionopause, the relation $[p + B^2/8\pi] = 0$ of (12) may be simplified to

$$p_{atm} = (p + B^2/8\pi)_{flow} \tag{17}$$

The variation of the pressure with radial distance from the planet center is given according to the hydrostatic equation by

$$dp/dr = -\rho g \tag{18}$$

where p and ρ are the ionized gas pressure and density, r is the radial distance measured from the center of the planet, and $g = |\underline{g}| = g_s(r_s/r)^2$, where subscript s denotes values at the surface of the planet. Combination of (18) and the perfect gas law given by (6) provides

$$p = p_R \exp\left(-\int_{R_R}^{r} \frac{dr}{H}\right) \tag{19}$$

where p_R is the pressure at some reference radius R_R and $H = \bar{R}T/\bar{M}g$ represents the local scale height of the ionospheric plasma.

If H is regarded as constant, i.e., if variations of g and T with r are disregarded, (19) can be integrated directly to obtain

$$p = p_R \exp\left(-\frac{r - R_R}{H}\right) \tag{20}$$

Because of limited knowledge of the ionospheric properties of Venus at the time, the simple variation of p with r given by (20) was adopted in the initial study of Spreiter et al. [1970] and also in the more recent analysis of Stahara et al. [1977] involving the initial application of advanced computational methods to this problem. Data from the Pioneer Venus spacecraft [Knudsen et al., 1979a, b] have provided much additional knowledge of conditions in the Venus ionosphere and, in particular, have shown that the assumption of an isothermal (T = const) ionosphere at the heights of concern here is quite reasonable. With this assumption, including the variation of

gravity with height, the following result for the pressure is obtained:

$$p = p_R \exp\left[-\frac{R_R \cdot (r - R_R)}{\bar{H} \cdot r}\right] \tag{21a}$$

where

$$\bar{H} = H_s \cdot (R_R/R_s)^2 \tag{21b}$$

R_s being the planetary radius and $H_s = \bar{R}T/\bar{M}g_s$. Equations (20) and (21) provide the two models employed in this study for the ionosphere pressure variation required in the pressure balance relation of (17).

On the basis of the typically hypersonic values for M_∞ it has been assumed in all the previous analyses cited above that the pressure of the solar wind plasma on the ionopause could be represented adequately by the Newtonian approximation

$$p = K\rho_\infty v_\infty^2 \cos^2\psi$$

$$K = \frac{1}{\gamma}\left[\frac{[(\gamma+1)/2]^{\gamma+1}}{\gamma-(\gamma-1)/2M_\infty^2}\right]^{\frac{1}{\gamma-1}} \tag{22}$$

where ψ is the angle between the outward normal to the ionopause and the flow direction of the undisturbed solar wind incident on the bow wave and K is a constant usually taken as one but whose actual value to provide the correct gasdynamic stagnation pressure at the nose of the ionopause is as indicated.

The Newtonian approximation stems from gasdynamic analysis of hypersonic flows and is appropriate in the range of ψ from 0° to somewhat less than 90°. In view of the close association between the magnetic pressure $B^2/8\pi$ and the gas pressure p in magnetohydrodynamics, it seems equally plausible to assume that the corresponding relation

$$p + B^2/8\pi = K\rho_\infty v_\infty^2 \cos^2\psi \tag{23}$$

is an appropriate, if not superior, relation for the combined magnetic and gas pressure of solar wind plasma on a planetary ionopause or magnetopause.

For the high Mach number flows typical of solar wind conditions, K approaches 0.881 for $\gamma = 5/3$ and 0.844 for $\gamma = 2$. A discussion of effects of minor constituents, such as ionized helium, in the solar wind and of some differences between a fluid and collisionless particle representation has been given by Spreiter [1976], but the most important effect of the introduction of the Newtonian approximation is that the calculation of the shape of the ionopause decouples from the calculation of the properties of the external flow. In this way we arrive at the following equation for the pressure balance at the ionopause location R_i:

$$K\rho_\infty v_\infty^2 \cos^2\psi = p_R A(R_i) \tag{24}$$

where

$$A(R_i) = \exp\left[-\left(\frac{R_i - R_R}{H}\right)\right] \qquad g, T = \text{const} \tag{25a}$$

or

$$A(R_i) = \exp\left[-R_R\left(\frac{R_i - R_R}{\bar{H} \cdot R_i}\right)\right] \qquad g = g_s\left(\frac{r_s}{r}\right)^2,\ T = \text{const} \tag{25b}$$

depending upon whether or not the gravitation variation is included in the scale height. It is convenient to choose the reference radius R_R to be the distance R_o from the center of the planet to the nose of the ionopause. Then $p_R = p_o = K\rho_\infty v_\infty^2$, and

$$\cos^2\psi = A(R_i) \tag{26}$$

at all points along the ionopause. To proceed, $\cos^2\psi$ must be expressed in terms of R_i and β, where $R_i(\beta)$ represents the radial coordinate of the ionopause and β is the angle measured at the center of the planet with respect to a line that extends directly upstream. The appropriate expression is [Spreiter et al., 1970]

$$\cos^2\psi = \left(\frac{dY_i}{dS}\right)^2 = \frac{(R_i d\beta \cos\beta + dR_i \sin\beta)^2}{dR_i^2 + (R_i d\beta)^2} \tag{27}$$

Substitution of this expression into (26) results in the following ordinary differential equation for the ordinates of the ionosphere boundary:

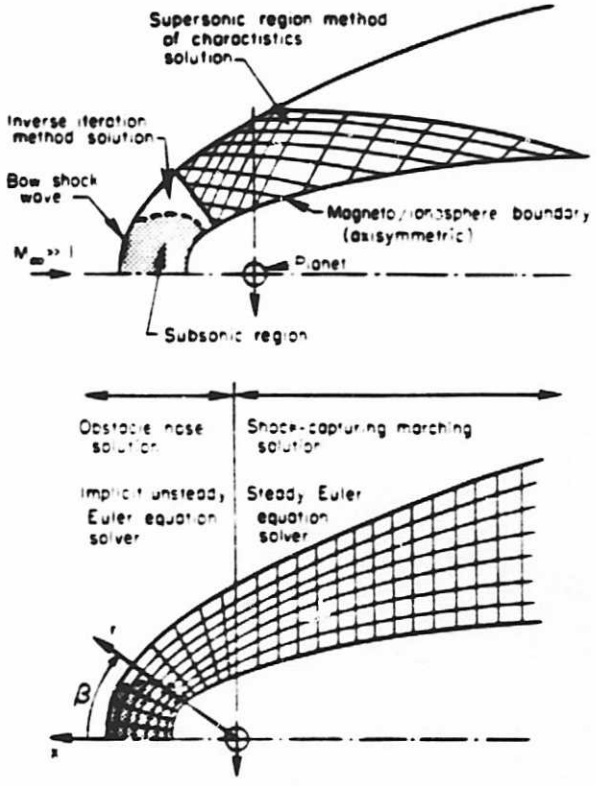

Fig. 3. Comparison of former and present computational procedures for determining the gasdynamic flow properties of solar wind-magneto/ionopause interactions.

$$\frac{dR_1}{d\beta} = R_1\left[\frac{\sin 2\beta - 2\sqrt{\Lambda - \Lambda^2}}{2(\Lambda - \sin^2\beta)}\right] \quad 0 \le \beta \le \pi \qquad (28)$$

Results for various ionopause shapes obtained by integrating (28) for different values of H/R_0 using the constant scale height model equation (25a) were provided by Spreiter et al. [1970]. Similar results using the isothermal model equation (25b) in the range $0.01 \le \bar{H}/R_0 \le 0.5$ are provided in Figure 2, where for comparison the constant scale height shapes for corresponding H/R_0 values are also illustrated. Data from Pioneer Venus indicate that the range of interest for application to Venus appears to be $0.01 \le \bar{H}/R_0 \le 0.10$. They also indicate that the theory provides a good representation of the ionopause shape on the dayside but that conditions on the nightside are both more complex and variable than presently accounted for by the theory (see, for example, Brace et al. [1979], Russell et al. [1979b], or Brace et al. (this issue). To provide insight into some of the changes to be encountered in the theory, some results are also included herein in which the nightside ionopause is arbitrarily flared in and out from the calculated shapes of Figures 1 and 2.

Calculation of the Gasdynamic Flow Properties

Determination of the gasdynamic flow properties is the most difficult and time-consuming portion of the numerical solution of the foregoing equations. As sketched in Figure 3, two different methods are used in the calculations: one for the nose region, where both subsonic and supersonic flows occur, and another downstream of that region, where a more computationally economical procedure can be employed, since the flow is everywhere supersonic. In the original analysis of Spreiter et al. [1970] an inverse iteration method was used for the nose region, and the method of characteristics was employed for the remaining supersonic region. Both of these procedures are inferior to more recently developed methods and have been superseded in the current model. The nose region is treated using a new axisymmetric implicit unsteady Euler equation solver specifically developed for the present application. That procedure determines the steady state solution in the nose region by an asymptotic time-marching procedure. The downstream solution is determined by a shock capturing marching procedure which spatially advances the solution downstream as far as required by solving the steady Euler equations. Inasmuch as these methods are complex and lengthy to describe, only an outline of the procedures is provided here.

The Nose Region Solution

The nose region procedure solves the unsteady gasdynamic equations (1), (6), (7), and (13)-(16) for axisymmetric flow. The analysis commences by mapping the portion of the ionosheath bounded by the stagnation streamline, the bow wave, the ionopause, and a line through the terminator ($\beta = \pi/2$) into a rectangle. The physical boundary conditions are also transferred appropriately. Initial flow field conditions are prescribed by using a linear variation of the flow properties between those calculated at an assumed location for the bow wave and those calculated at the ionopause, using a Newtonian pressure distribution approximation on the latter boundary. Starting with this initial flow, the unsteady equations are integrated in a time-asymptotic fashion until the steady state solution is obtained.

The basic numerical algorithm employed was developed by Beam and Warming [1976] and is second-order accurate, noniterative, and spatially factored. At the ionopause and bow shock boundaries a modification of the differencing algorithm is introduced to account for the particular features of the present application. The tangency condition at the ionopause is treated using the method of Kentzer [1970], and the sharp discontinuity approach of Thomas et al. [1972] is used at the bow wave. Any secondary shocks which may occur in the nose region are automatically determined via the shock-capturing characteristics of the algorithm.

In our earlier work [Stahara, et al., 1977] it was found that for certain ionopause shapes which have a significant amount of lateral flaring at the dawn-dusk terminator, for example, constant scale height shapes for $H/R_0 \ge 0.5$, and/or cases involving low free-stream Mach numbers $M_\infty \le 3$, the axial component of velocity at some points on the terminator plane $\beta = \pi/2$ may become subsonic. Although this has no effect on the nose region solver, the downstream solution cannot be obtained for these cases, since the marching-region solver which determines the solution downstream of this starting plane requires supersonic axial velocities in order to proceed. In the present effort this limitation has been removed by developing the capability for adding an additional portion of the flow field, located downstream of the terminator, to the blunt body solution as illustrated in Figure 4. This effectively generalizes the capability of the present procedures to treat a wide variety of ionopause shapes, including all of the shapes described by the constant scale height and constant temperature models found using (25a) and (25b), as well as to treat lower free-stream Mach numbers down to about $M_\infty = 2$.

The Downstream Region Solution

The solver for the downstream supersonic region is based on the original work of Kutler et al. [1972, 1973] and Chaussee et al. [1975] and solves for axisymmetric flow the steady state gasdynamic equations in conservation law form indicated by (1), (6), (7), and (13)-(16) with the time derivatives set to zero. Of these, (14), which represents the conservation of energy, can be integrated for the steady flow to yield the following equation for the total enthalpy:

$$h_t = h + (u^2 + v^2)/2 = \text{const} \qquad (29)$$

where $h = e + p/\rho = C_pT$ is the enthalpy per unit mass. This relation also holds in the nose region in the limit as the steady state flow solution is approached. The computational mesh defined by lines of constant X and $(R - R_b)/(R_s - R_b)$, where R_s and R_b are functions of X that describe the radial cylindrical coordinates of the bow shock

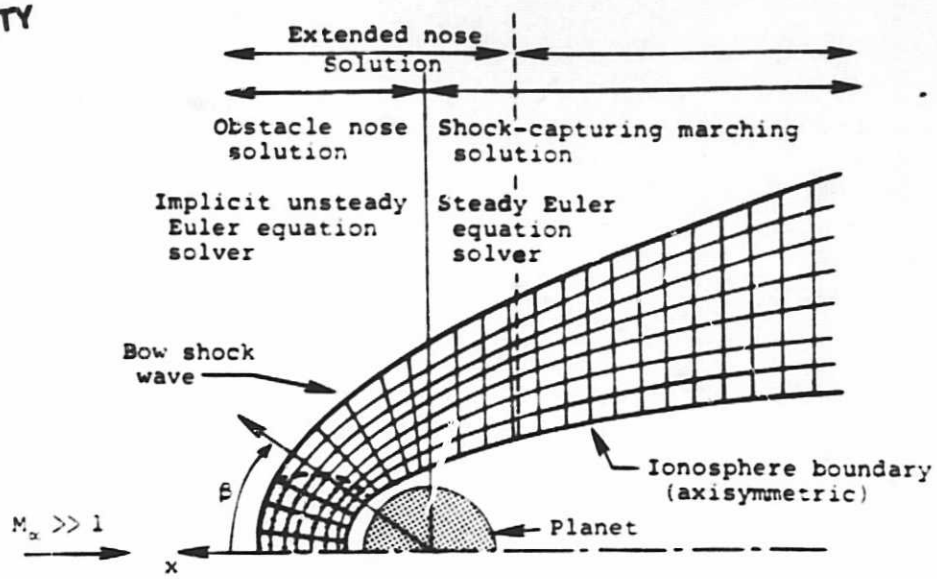

Fig. 4. Illustration of additional flow field segment to the obstacle nose solution for determining the gasdynamic flow properties of solar wind-ionopause interactions.

wave and ionopause at the same X as the field point (X, R), is transformed into a rectangular computational grid. The gasdynamic equations are similarly transformed and integrated numerically to obtain the solution. Since only the bow shock wave is treated as a sharp discontinuity and any others that may be present are 'captured' by the difference algorithm, selection of the appropriate finite difference scheme to advance the calculation in the X direction is of prime importance. Following the analysis of Kutler et al. [1972, 1973] and Chaussee et al. [1975] the method used is the finite difference predictor-corrector scheme of MacCormack [1969], the most efficient second-order algorithm for shock-capturing calculations.

Calculation of the Streamlines

The accurate determination of the gasdynamic streamlines is crucial, since they provide the basis for the frozen magnetic field calculation described in the following section. The streamlines are determined by integrating fluid particle trajectories through the known velocity field, since this procedure was found to be more accurate than the alternative mass flow calculation. The calculation of a particular streamline is initiated at the point where the streamline crosses the bow shock. At that point, exact values of the streamline slope dR_S/dX are given by the following relation involving M_∞, γ, and the angle δ_S between the free-stream direction and the tangent to the shock wave:

$$\frac{dR_S}{dX} = \frac{(2\cot\delta_S)(M_\infty^2\sin^2\delta_S - 1)}{2 + M_\infty^2(\gamma + 1 - 2\sin^2\delta_S)} \tag{30}$$

which is contained implicitly in both nose and marching region gasdynamic solutions. At other points, the local streamline slope is given by the ratio

$$dR_S/dX = v/u \tag{31}$$

and the streamline determination is made by stepwise integration in X using a modified third-order Euler predictor-corrector method. Bivariate linear interpolation between the flow field grid points is employed to obtain the velocity components (u, v) required at the stepwise points along the streamline.

Calculation of the Magnetic Field

With the flow properties known from the gasdynamic calculations, the magnetic field $\underset{\sim}{B}$ may be determined by integrating (4) and (10); or alternatively, the following equations may be derived from them:

$$\frac{D}{Dt}\iint_S \underset{\sim}{B}\cdot d\underset{\sim}{S} = 0 \qquad \frac{D}{Dt}\left(\frac{\underset{\sim}{B}}{\rho}\right) = \frac{1}{\rho}(\underset{\sim}{B}\cdot\underset{\sim}{\nabla})\underset{\sim}{v} \tag{32}$$

in which S is an arbitrary surface moving with the fluid and D/Dt is the material or substantial derivative $dD/Dt = \partial/\partial t + (\underset{\sim}{v}\cdot\underset{\sim}{\nabla})$. These equations are commonly interpreted as indicating the field lines move with the fluid. For the steady state in which $\partial/\partial t = 0$ and $v_n^* = v_n$, these equations lead to a straightforward calculation in which the vector distance from each point on an arbitrarily selected field line to its corresponding point on an adjacent field line in the downstream direction is determined by numerically integrating $\int \underset{\sim}{v}\, dt$ over a fixed time interval Δt as indicated in Figure 5. Once the magnetic field lines are

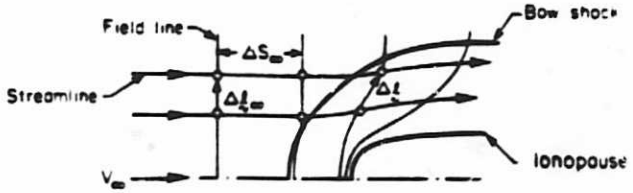

Fig. 5. Illustration of quantities used for magnetic field line calculation in the plane of magnetic symmetry.

determined, the magnetic field at any point may be calculated from the relation

$$\frac{\underset{\sim}{B}}{|\underset{\sim}{B}_\infty|} = \frac{\rho}{\rho_\infty}\frac{\Delta\underset{\sim}{\ell}}{|\Delta\underset{\sim}{\ell}_\infty|} \tag{33}$$

where $\Delta\underset{\sim}{\ell}$ is the vector length of a small element of a flux tube.

Such a procedure is valid generally, but its use is confined in the present calculation to only the component of the magnetic field ($\underset{\sim}{B}$) that lies in the plane of magnetic symmetry defined by the plane containing the axis of symmetry of the ionopause and the magnetic field lines upstream of the bow wave and furthermore is associated with only the component of the interplanetary magnetic field that lies in the plane of magnetic symmetry and is perpendicular to $\underset{\sim}{v}_\infty$. The remainder of the magnetic field calculation makes use of a decomposition due to Alksne and Webster [1970] in which the axisymmetric properties of the gasdynamic solution and the linearity of the magnetic field equations (4) and (10) or (32) are employed to derive the following relationship for the magnetic field $\underset{\sim}{B}_P$ at any point P:

$$\underset{\sim}{B}_P = \left(\frac{\underset{\sim}{B}_P}{\underset{\sim}{B}_\infty}\right)_{\!\!\shortparallel} \underset{\sim}{B}_{\infty\shortparallel} + \left(\frac{\underset{\sim}{B}_P}{\underset{\sim}{B}_\infty}\right)_{\!\!\perp} \underset{\sim}{B}_{\infty\perp} + \hat{e}_n \left(\frac{\underset{\sim}{B}_P}{\underset{\sim}{B}_\infty}\right)_{\!\!n} B_{\infty n} \tag{34}$$

As illustrated in Figure 6, subscripts $\shortparallel$, $\perp$, and n refer to contributions associated with the component $\underset{\sim}{B}_{\infty\shortparallel}$ of $\underset{\sim}{B}_\infty$ parallel to $\underset{\sim}{v}_\infty$; the component $\underset{\sim}{B}_{\infty\perp}$ perpendicular to $\underset{\sim}{v}_\infty$ in the plane that contains the point P, the center of the planet, and the vector $\underset{\sim}{v}_\infty$; and the component $B_{\infty n}$ normal to the latter plane, where $\hat{e}_n$ is a unit vector in the latter direction. The unit ratios $(\underset{\sim}{B}_P/\underset{\sim}{B}_\infty)_\shortparallel$ and $(\underset{\sim}{B}_P/\underset{\sim}{B}_\infty)_n$ can be calculated directly from the gasdynamic solution by the expressions

$$\left(\frac{\underset{\sim}{B}_P}{\underset{\sim}{B}_\infty}\right)_{\!\!\shortparallel} = \frac{\rho_P \underset{\sim}{v}_P}{\rho_\infty |\underset{\sim}{v}_\infty|}, \qquad \left(\frac{\underset{\sim}{B}_P}{\underset{\sim}{B}_\infty}\right)_{\!\!n} = \frac{R_P \rho_P}{R_{P_\infty}\rho_\infty} \tag{35}$$

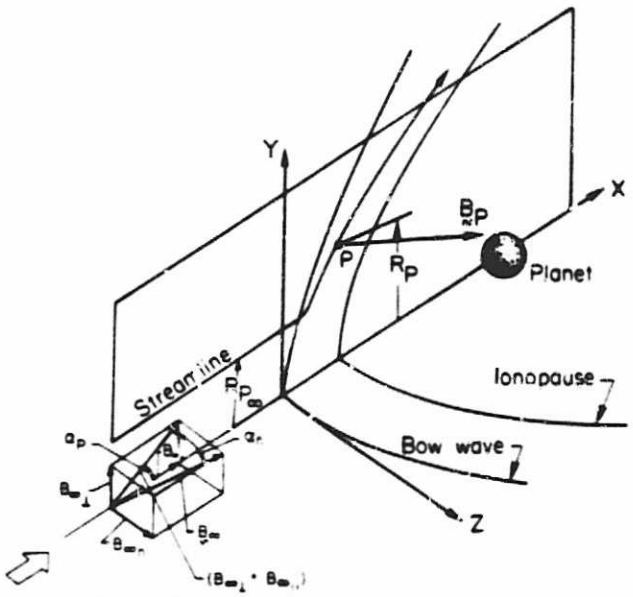

Fig. 6. Illustration of the components of the three-dimensional magnetic field.

where R_P is the radial cylindrical coordinate of the streamline through P, as indicated in Figure 6.

In carrying out the determination of $(\underset{\sim}{B}_P/\underset{\sim}{B}_\infty)_\perp$ using (33), values for $\Delta\underset{\sim}{\ell}/|\Delta\underset{\sim}{\ell}_\infty|$ are determined initially at the points where the streamlines and perpendicular-component field lines intersect. A generalized quadrilateral interpolation scheme followed by a fifth-order smoothing is then employed to determine the corresponding values at the computational grid points where values for ρ/ρ_∞ are available for calculation of $(\underset{\sim}{B}_P/\underset{\sim}{B}_\infty)_\perp$. At the bow shock, exact formulas are used for the magnitude and direction of $\Delta\underset{\sim}{\ell}$:

$$\begin{aligned}(|\Delta\underset{\sim}{\ell}|/|\Delta\underset{\sim}{\ell}_\infty|)^2 &= 1 + \cot^2\theta(1+D^2) \\ &\quad - 2D \times \csc\theta \times \cot\theta \times \cos(\theta-\delta) \\ \psi &= \theta + \sin^{-1}\{[D \times \cot\theta \\ &\quad \times \sin(\theta-\delta)]/(|\Delta\underset{\sim}{\ell}|/|\Delta\underset{\sim}{\ell}_\infty|)\}\end{aligned} \tag{36}$$

where

$$\begin{aligned}D^2 &= 1 - 4(M_\infty^2\sin^2\theta - 1) \\ &\quad \times (\gamma M_\infty^2\sin^2\theta + 1)/[(\gamma+1)^2 M_\infty^4\sin^2\theta] \\ \cot\delta &= \left[(\gamma+1)M_\infty^2/[2(M_\infty^2\sin^2\theta - 1)] - 1\right]\tan\theta \\ \theta &= \tan^{-1}\left(\frac{dR_S}{dX}\right)\end{aligned} \tag{37}$$

and ψ is the angle between the free-stream direction and the $\Delta\underset{\sim}{\ell}$ vector.

Finally, the resultant magnetic field vector can be expressed in terms of components relative to any orthogonal (X, Y, Z) coordinate system. If the coordinate system is oriented so that the point P lies in the (X, Y) plane, the magnetic components are

$$\begin{aligned}B_X/B_\infty &= [(|\underset{\sim}{B}|/B_\infty)_\shortparallel \cos\phi\cos\alpha_p \\ &\quad + (|\underset{\sim}{B}|/B_\infty)_\perp \cos\psi\sin\alpha_p)]\cos\alpha_n \\ B_Y/B_\infty &= [(|\underset{\sim}{B}|/B_\infty)_\shortparallel \sin\phi\cos\alpha_p \\ &\quad + (|\underset{\sim}{B}|/B_\infty)_\perp \sin\psi\sin\alpha_p)]\cos\alpha_n \\ B_Z/B_\infty &= (B/B_\infty)_n \sin\alpha_n\end{aligned} \tag{38}$$

where ϕ is the local flow angle given by

$$\phi = \tan^{-1}\left(\frac{v}{u}\right) \tag{39}$$

and the interplanetary magnetic field angles α_p and α_n indicated in Figure 6 are defined by

$$\alpha_p = \tan^{-1}\left[\frac{B_{\infty\perp}}{B_{\infty\shortparallel}}\right] = \tan^{-1}\left[\frac{B_{Y_\infty}}{B_{X_\infty}}\right] \tag{40}$$

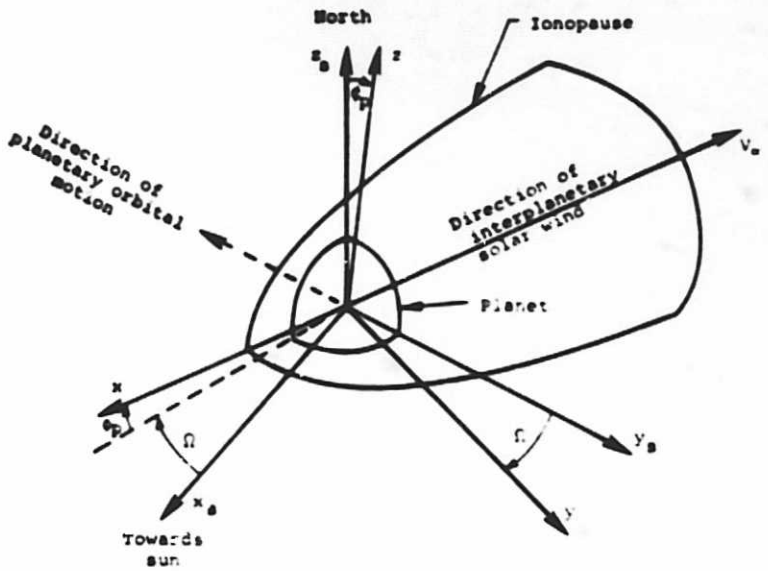

Fig. 7. Illustration of sun-planet (x_s, y_s, z_s) and solar wind (x, y, z) coordinate systems and the azimuthal (Ω) and polar (ϕ_p) solar wind angles, both shown in a positive sense.

$$\alpha_n = \tan^{-1}\left[\frac{B_{\infty_n}}{\sqrt{(B_{\infty_{\parallel}})^2 + (B_{\infty_{\perp}})^2}}\right] = \tan^{-1}\left[\frac{B_{Z_\infty}}{\sqrt{(B_{X_\infty})^2 + (B_{Y_\infty})^2}}\right] \quad (41)$$

The generalization of these results when the point P is at some arbitrary (X, Y, Z) point not in the (X, Y) plane are provided below in the spacecraft trajectory section.

Calculation of the Contour Lines

In order to provide convenient summary information of the detailed plasma and magnetic field properties determined by the above model, contour and field line maps are determined for the important field properties. Contours are calculated for nondimensionalized velocity $|\underset{\sim}{v}|/v_\infty$, density ρ/ρ_∞, and magnetic field components $(|\underset{\sim}{B}|/B_\infty)_{\parallel}$, $(|\underset{\sim}{B}|/B_\infty)_{\perp}$ and $(B/B_\infty)_n$. Details of these calculations are provided by Stahara et al. [1980]. Since the temperature is a function of $|\underset{\sim}{v}|/v_\infty$ only for a specified M_∞ and γ, i.e.,

$$T/T_\infty = 1 + \left(\frac{\gamma-1}{2}\right) M_\infty^2 \left[1 - \left(\frac{|\underset{\sim}{v}|}{v_\infty}\right)^2\right] \quad (42)$$

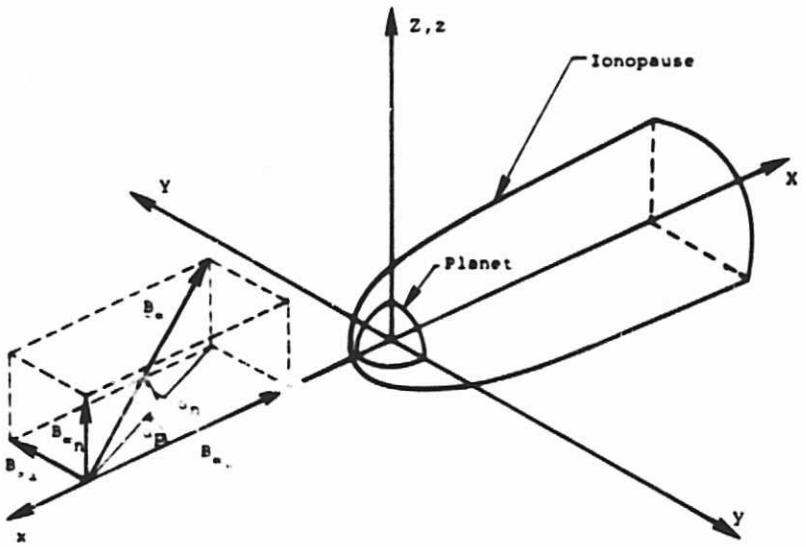

Fig. 8. Illustration of solar wind (x, y, z) and (X, Y, Z) coordinate systems and the interplanetary magnetic field and magnetic field angles (α_p, α_n).

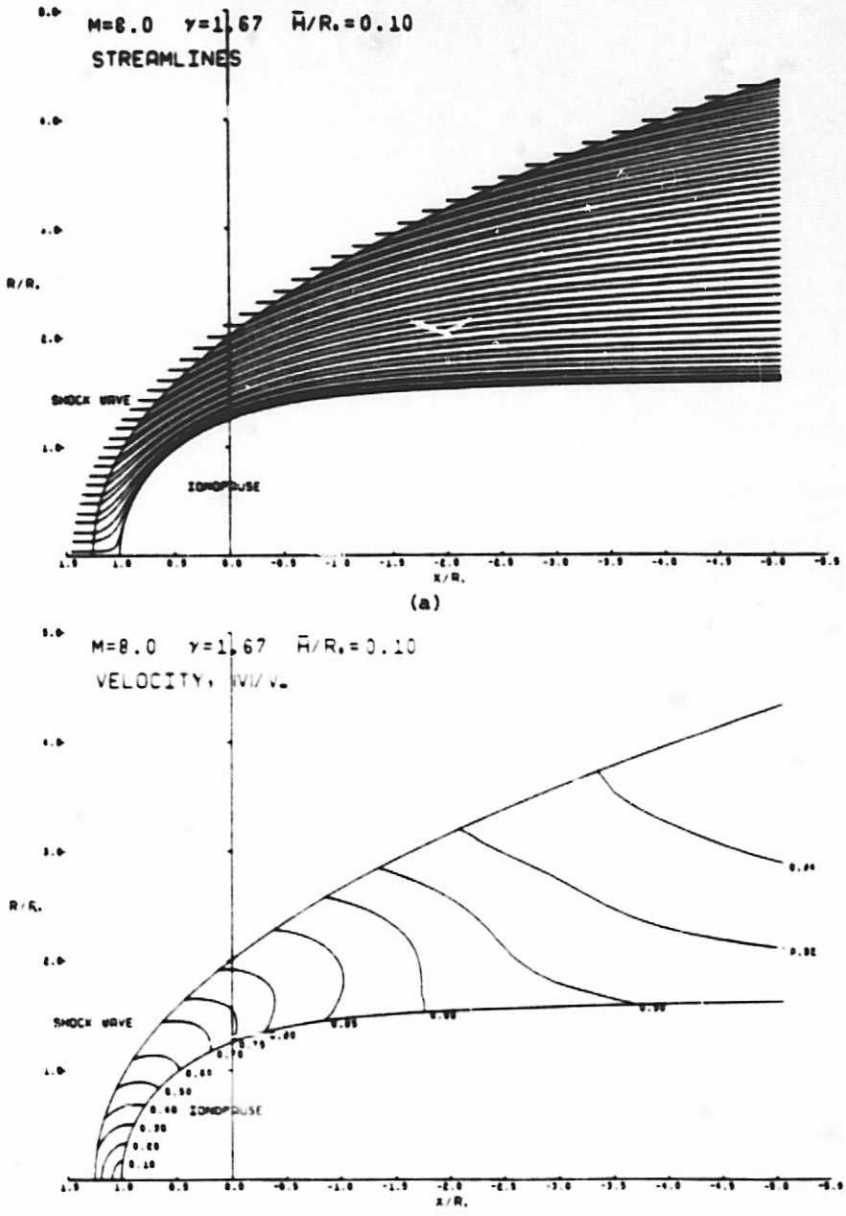

Fig. 9. Calculated ionopause and bow shock locations and ionosheath properties for $M_\infty = 8.0$, $\gamma = 5/3$, $\bar{H}/R_0 = 0.10$, and B_∞ either parallel or perpendicular to V_∞. (a) Streamline map. (b) Velocity map, (c) Density map, (d) Temperature map. (e) Parallel magnetic field map. (f) Perpendicular magnetic field map.

velocity contours may also be considered as temperature contours with only a relabeling required.

Solar Ecliptic/Solar Wind Coordinate Transformation

To compare results of the present calculations with observational data, it is necessary to consider the appropriate transformations between the spacecraft and solar wind coordinate systems. Part of the data required as input to the theoretical model consists of oncoming interplanetary values of solar wind temperature, density, and velocity and magnetic field vector components. These are usually reported in a sun-planet or solar ecliptic reference frame, whereas the natural coordinate system for the theoretical model is one which aligns the axial direction with the oncoming solar wind, since the gasdynamic calculation is assumed to be axisymmetric about this direction. Thus the interplanetary input data must be transformed to the solar wind system to initiate the theoretical determination. Once the gasdynamic and magnetic field calculations in the solar wind system are complete, those results must then be transformed back to the sun-planet system to allow direct comparison with the spacecraft data obtained as a function of time along its trajectory.

For the sun-planet system (x_s, y_s, z_s) the

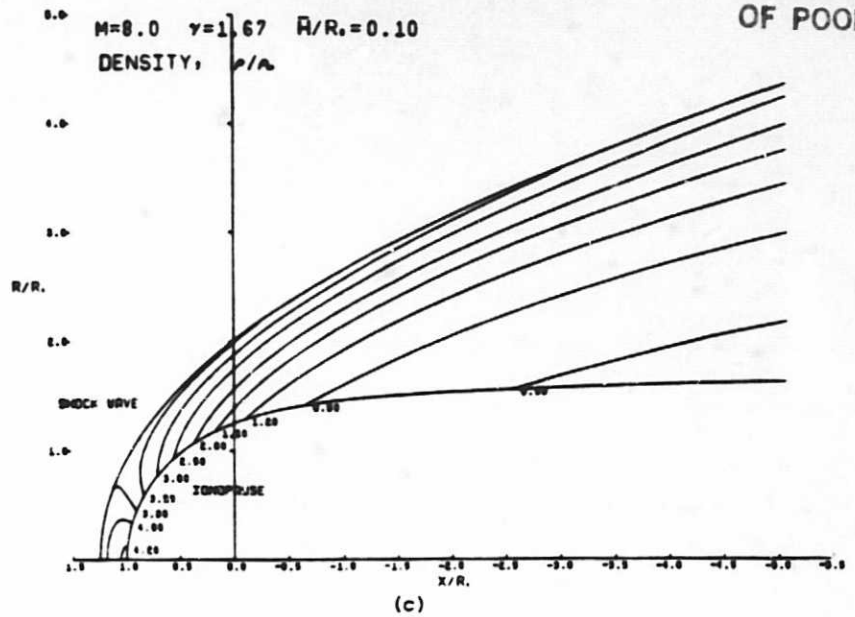

(c)

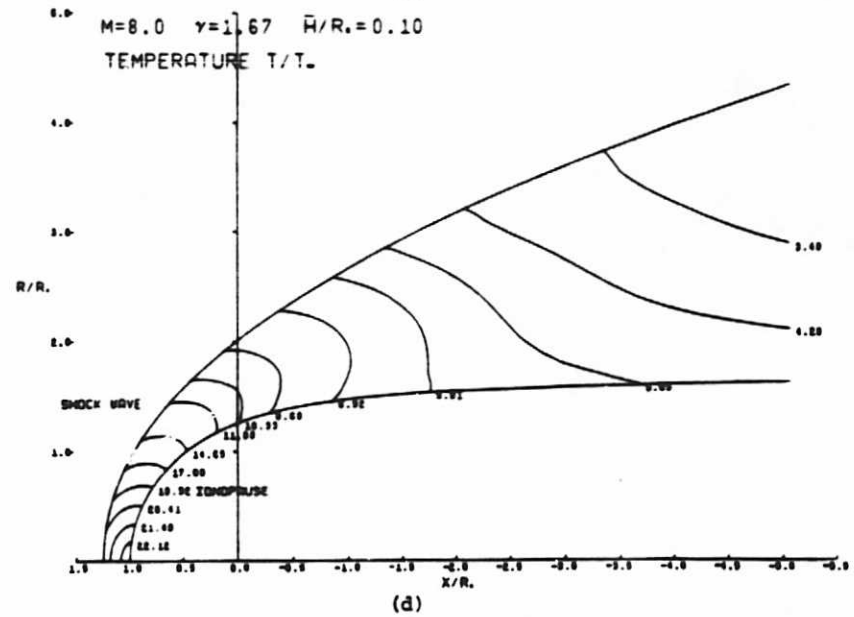

(d)

Fig. 9. (continued)

origin is placed at the planetary center, the x_s axis is directed toward the sun, the y_s axis is directed opposite to the planetary orbital motion, and the z_s axis is orthogonally northward. The direction of the oncoming solar wind is such that the azimuthal angle, including aberration effects due to planetary motion, of the solar wind velocity vector in the planetary orbital plane is Ω, and the out-of-orbital plane polar angle is ϕ_p. The positive sense of the azimuthal angle is for west-to-east flow, and that of the polar angle is for north-to-south flow, as indicated in Figure 7. Also illustrated is the solar wind (x, y, z) coordinate system defined by (Ω, ϕ_p). This system is somewhat inconvenient because the direction of solar wind flow is in the negative x direction; therefore the internal gasdynamic and magnetic field calculations are performed in the (X, Y, Z) system illustrated in Figure 8.

The coordinates and vector transformations from the ecliptic sun-planet (x_s, y_s, z_s) system to the (X, Y, Z) solar wind system are given by

$$\begin{pmatrix} Q_X \\ Q_Y \\ Q_Z \end{pmatrix} = \begin{bmatrix} -\cos\Omega\cos\phi_p & -\sin\Omega\cos\phi_p & \sin\phi_p \\ \sin\Omega & -\cos\Omega & 0 \\ -\cos\Omega\sin\phi_p & \sin\Omega\sin\phi_p & \cos\phi_p \end{bmatrix} \begin{pmatrix} Q_{x_s} \\ Q_{y_s} \\ Q_{z_s} \end{pmatrix} \quad (43)$$

where (Q_X, Q_Y, Q_Z) represents the Cartesian components of any vector referred to the (X, Y, Z) system, and (Q_{x_s}, Q_{y_s}, Q_{z_s}) represents the corresponding vector in the (x_s, y_s, z_s) system. Thus for a transformation of coordinates,

$$\begin{aligned} (Q_x, Q_y, Q_z) &= (X, Y, Z) \\ (Q_{x_s}, Q_{y_s}, Q_{z_s}) &= (x_s, y_s, z_s) \end{aligned} \quad (44)$$

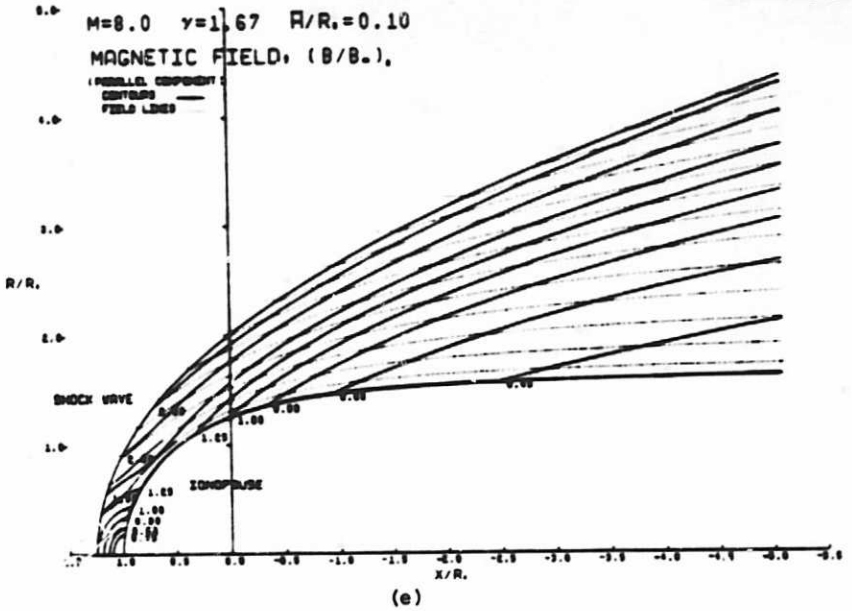

(e)

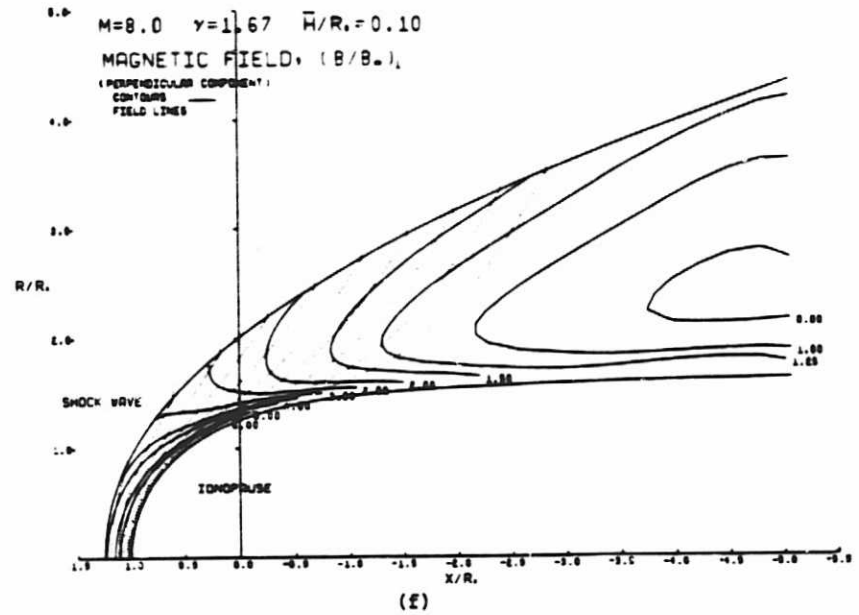

(f)

Fig. 9. (continued)

while for a vector transformation of, say, the magnetic field,

$$(Q_x, Q_y, Q_z) = (B_x, B_y, B_z)$$
$$(Q_{x_s}, Q_{y_s}, Q_{z_s}) = (B_{x_s}, B_{y_s}, B_{z_s}) \tag{45}$$

The inverse transformation from the solar wind to the sun-planet system is given by

$$\begin{pmatrix} Q_{x_s} \\ Q_{y_s} \\ Q_{z_s} \end{pmatrix} = \begin{pmatrix} -\cos\Omega\cos\phi_p & \sin\Omega & -\cos\Omega\sin\phi_p \\ \sin\Omega\cos\phi_p & -\cos\Omega & \sin\Omega\sin\phi_p \\ \sin\phi_p & 0 & \cos\phi_p \end{pmatrix} \begin{pmatrix} Q_X \\ Q_Y \\ Q_Z \end{pmatrix} \tag{46}$$

Properties Along a Spacecraft Trajectory

One of the primary aims of the present effort has been to develop the capability to determine plasma and magnetic field properties, as predicted by the theoretical model, at locations specified along an arbitrary spacecraft trajectory, and in such a form as to enable comparisons to be made directly with actual spacecraft data. To accomplish this, the following procedure has been developed and implemented in the current model. First, from the known oncoming interplanetary conditions provided in a sun-planet reference frame, the azimuthal and polar solar wind angles (Ω, ϕ_p) are employed in (43) to establish both the location (X_p, Y_p, Z_p) of the trajectory point and the interplanetary magnetic field components (B_{X_∞}, B_{Y_∞}, B_{Z_∞}) in the solar wind (X, Y, Z) frame.

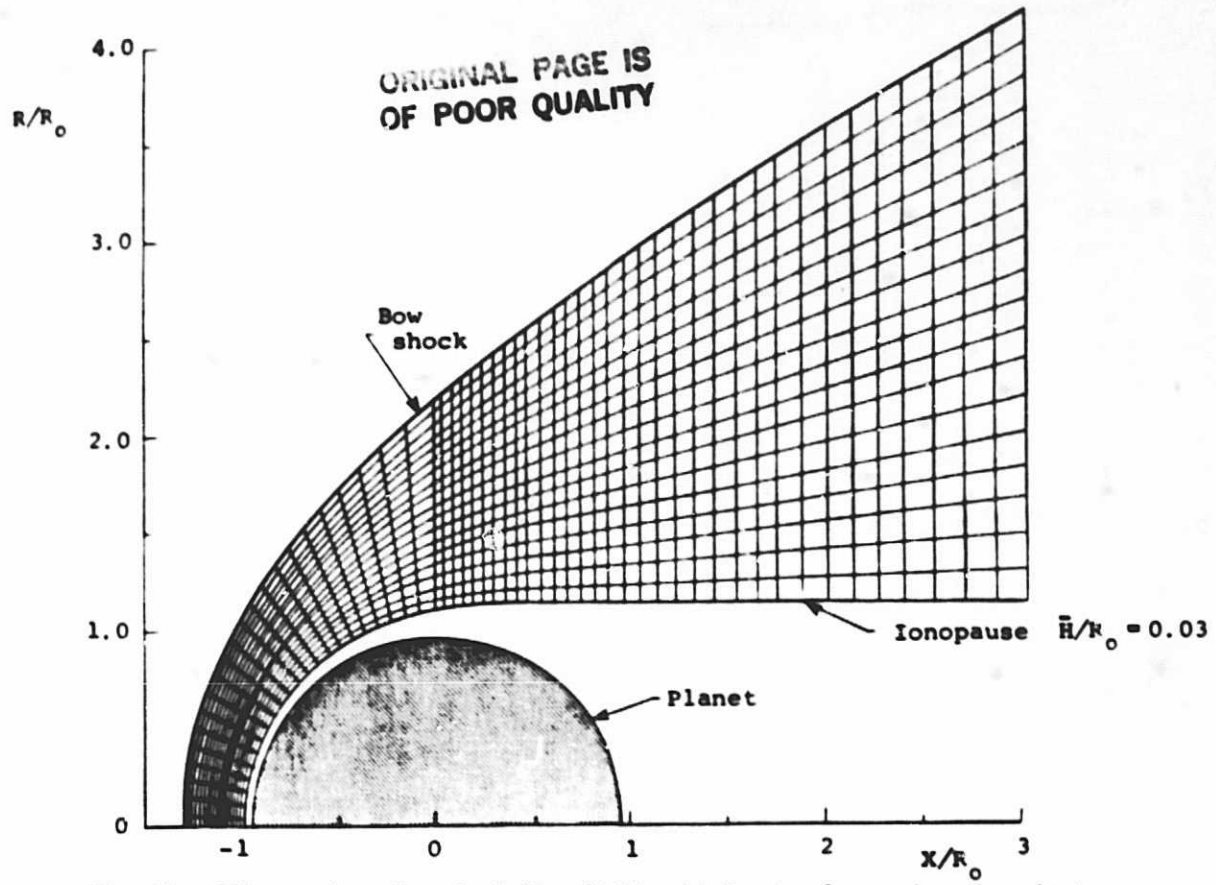

Fig. 10. Illustration of typical flow field grid density for gasdynamic solution; $M_\infty = 3.0$, $\gamma = 5/3$.

In the next step, in which the axisymmetric gasdynamic and unit magnetic field calculations are carried out, it is convenient to take advantage of the axisymmetric property of the gasdynamic flow and introduce still another coordinate system (X, y', z') related to the (X, Y, Z) system by a rotation about the X axis by an angle θ such that the y' axis passes through the point P. This rotation defines a new coordinate system (x', y', z'), where

$$\begin{pmatrix} x' \\ y' \\ z' \end{pmatrix} = \begin{pmatrix} 1 & 0 & 0 \\ 0 & \cos\theta & \sin\theta \\ 0 & -\sin\theta & \cos\theta \end{pmatrix} \begin{pmatrix} X \\ Y \\ Z \end{pmatrix} \tag{47}$$

in which

$$\theta = \tan^{-1}\left[\frac{Z_p}{Y_p}\right] \tag{48}$$

and

$$\begin{aligned} x' &= X_p \\ y' &= \sqrt{Y_p^2 + Z_p^2} \\ z' &= 0 \end{aligned} \tag{49}$$

Thus the (x', y') plane which contains the X axis and the arbitrary point P corresponds directly to the plane (X, R) = $(X_p, \sqrt{Y_p^2 + Z_p^2})$, in which the axisymmetric gasdynamic flow properties are calculated. In particular, the velocity magnitude v, density ρ, and flow angle ϕ at the point P are found by bilinear interpolation through the (X, R) flow field grid. The vector velocity in the (X, Y, Z) system is then given by the transformation

$$\begin{pmatrix} v_X \\ v_Y \\ v_Z \end{pmatrix} = \begin{pmatrix} 1 & 0 & 0 \\ 0 & \cos\theta & -\sin\theta \\ 0 & \sin\theta & \cos\theta \end{pmatrix} \begin{pmatrix} v\cos\phi \\ v\sin\phi \\ 0 \end{pmatrix} \tag{50}$$

and then in the solar ecliptic system by the transformation indicated by

$$\begin{pmatrix} v_{x_s} \\ v_{y_s} \\ v_{z_s} \end{pmatrix} = \begin{pmatrix} -\cos\Omega\cos\phi_p & \sin\Omega & -\cos\Omega\sin\phi_p \\ \sin\Omega\cos\phi_p & -\cos\Omega & \sin\Omega\sin\phi_p \\ \sin\phi_p & 0 & \cos\phi_p \end{pmatrix} \begin{pmatrix} v_X \\ v_Y \\ v_Z \end{pmatrix} \tag{51}$$

Calculation of the magnetic field at an arbitrary point is somewhat more complicated, since these components are dependent upon the orientation of the incident interplanetary mag-

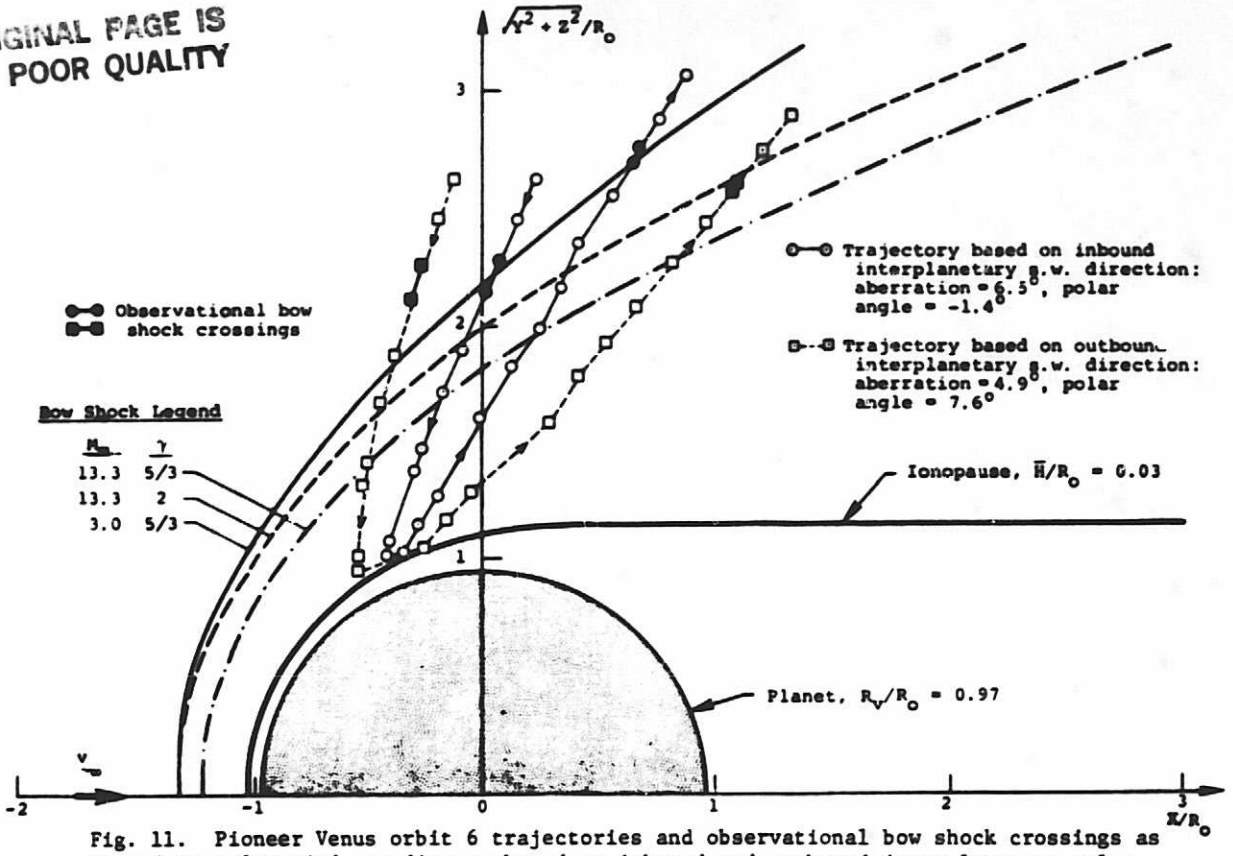

Fig. 11. Pioneer Venus orbit 6 trajectories and observational bow shock crossings as viewed in solar wind coordinates based on inbound and outbound interplanetary solar wind directions; also, various bow shock shapes for different interplanetary solar wind conditions.

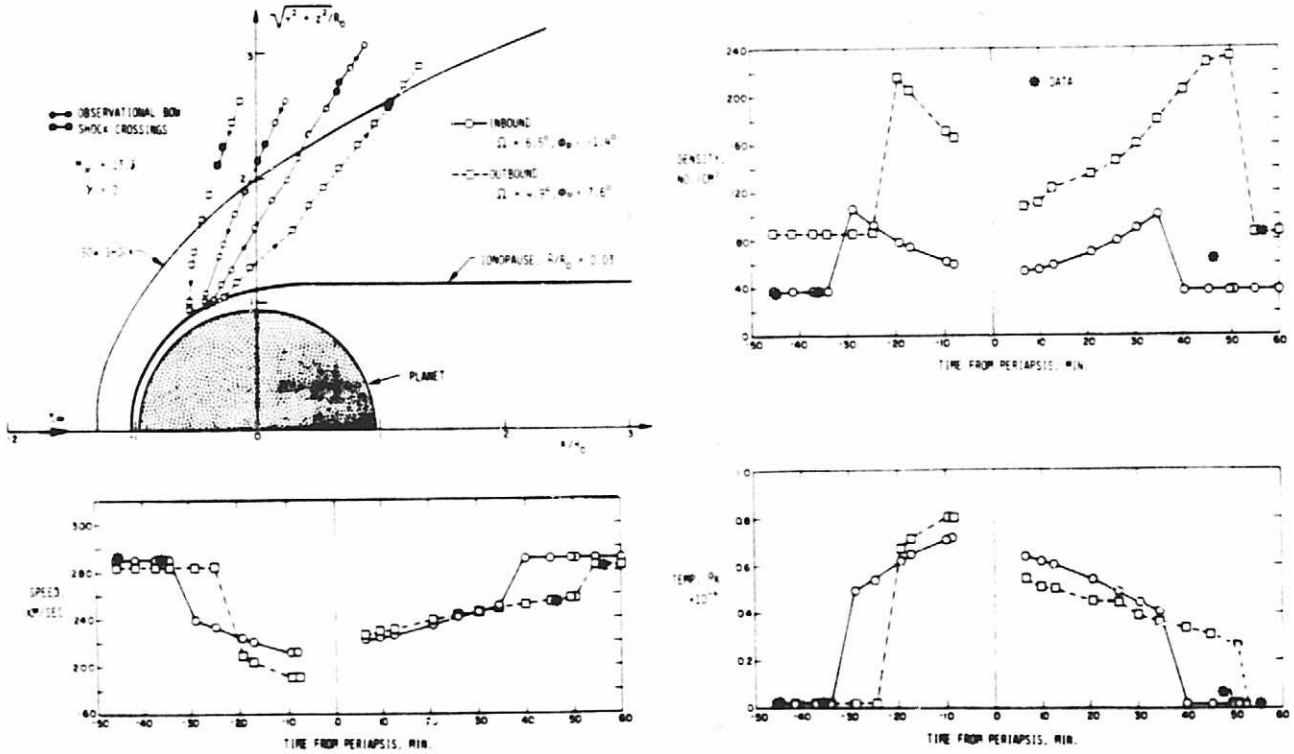

Fig. 12. Comparison of observed (OPA) and theoretical time histories of ionosheath plasma properties for Pioneer Venus orbit 6 based on inbound and outbound interplanetary solar wind conditions using a gasdynamic solution for M_∞ = 13.3, γ = 2.0.

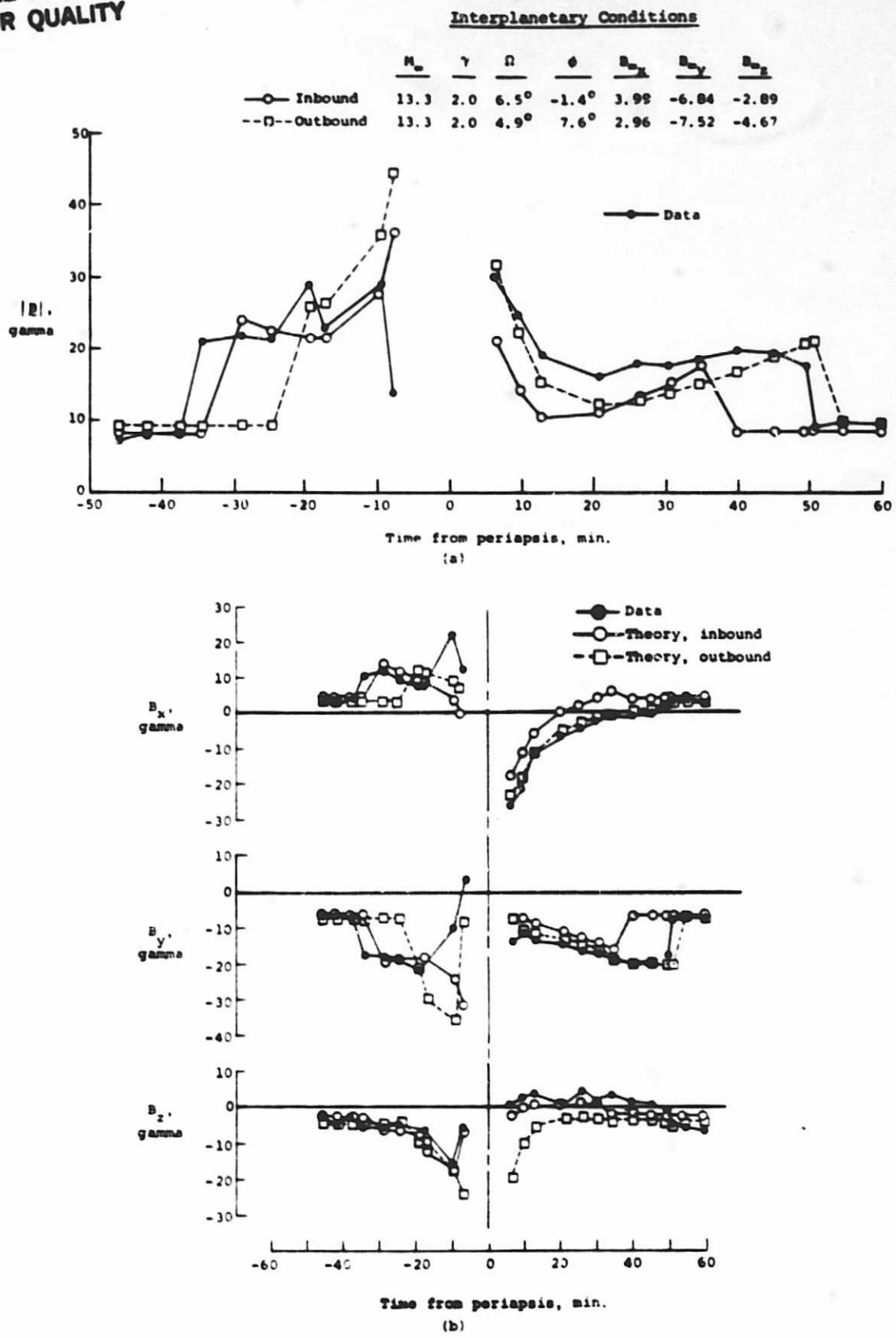

Fig. 13. Comparison of observed (OMAG) and theoretical time histories for the magnitude of the magnetic field for Pioneer Venus orbit 6 based on inbound and outbound interplanetary conditions using gasdynamic solution for $M_\infty = 13.3$, $\gamma = 2.0$. (a) Magnetic field magnitude. (b) Magnetic field components.

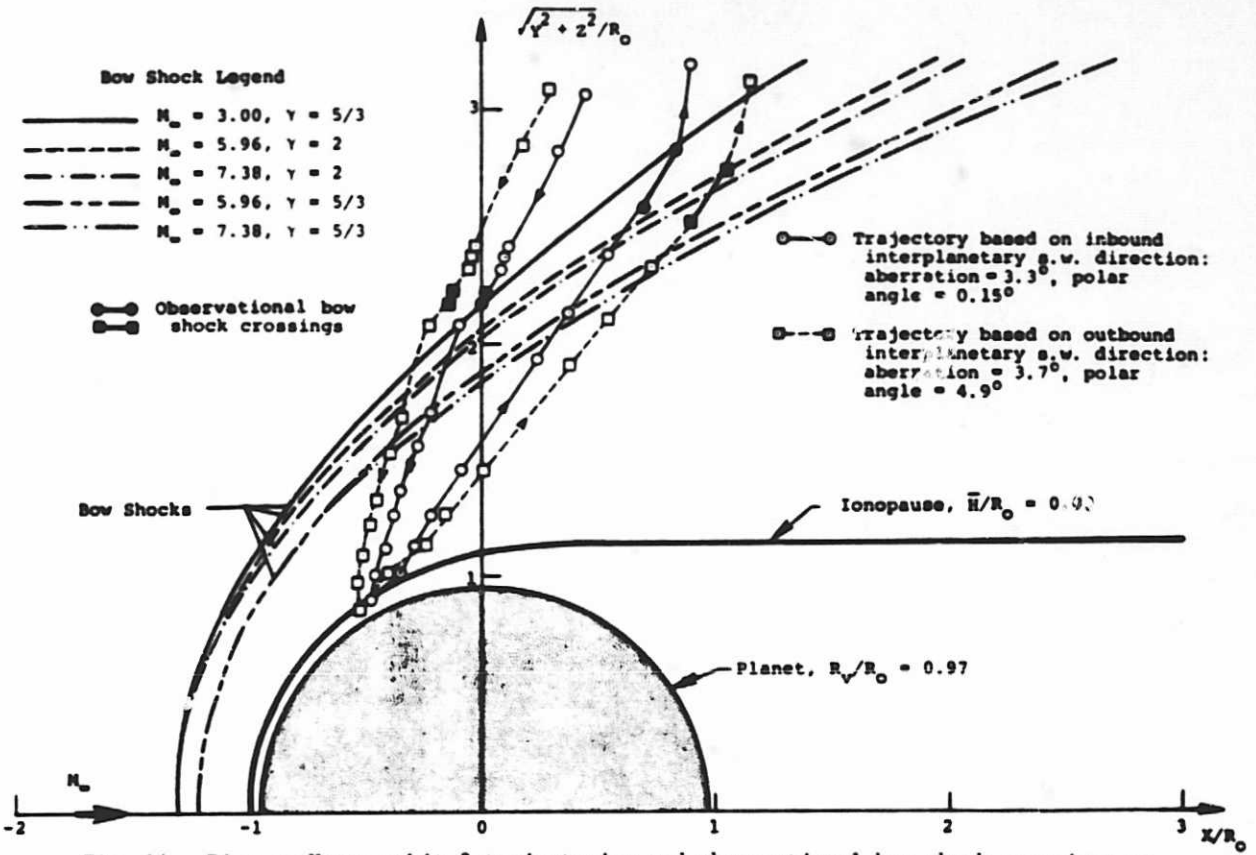

Fig. 14. Pioneer Venus orbit 3 trajectories and observational bow shock crossings as viewed in solar wind coordinates based on inbound and outbound interplanetary solar wind directions; also, various bow shock shapes for different interplanetary solar wind conditions.

netic field. With the known (B_X , B_Y , B_Z) components the corresponding components (B'_{x_∞}, B'_{y_∞}, B'_{z_∞}) in the rotated system are given by

$$\begin{pmatrix} B'_{x_\infty} \\ B'_{y_\infty} \\ B'_{z_\infty} \end{pmatrix} = \begin{pmatrix} 1 & 0 & 0 \\ 0 & \cos\theta & \sin\theta \\ 0 & -\sin\theta & \cos\theta \end{pmatrix} \begin{pmatrix} B_{X_\infty} \\ B_{Y_\infty} \\ B_{Z_\infty} \end{pmatrix} \tag{52}$$

In this reference frame the parallel, perpendicular, and normal interplanetary components are identified as

$$\begin{aligned} B_{\infty_\parallel} &= B'_{x_\infty} \\ B_{\infty_\perp} &= B'_{y_\infty} \\ B_{\infty_n} &= B'_{z_\infty} \end{aligned} \tag{53}$$

The magnetic field angles α'_p and α'_n in the rotated system are given by

$$\alpha'_p = \tan^{-1}\left[\frac{B_{\infty_\perp}}{B_{\infty_\parallel}}\right] = \tan^{-1}\left[\frac{B'_{y_\infty}}{B'_{x_\infty}}\right] \tag{54}$$

$$\begin{aligned} \alpha'_n &= \tan^{-1}\left[\frac{B_{\infty_n}}{\sqrt{(B_{\infty_\parallel})^2 + (B_{\infty_\perp})^2}}\right] \\ &= \tan^{-1}\left[\frac{B'_{z_\infty}}{\sqrt{(B'_{x_\infty})^2 + (B'_{y_\infty})^2}}\right] \end{aligned} \tag{55}$$

The magnetic angle ψ associated with the incident perpendicular component and the unit magnetic field ratios $(|\underset{\sim}{B}|/B_\infty)_\parallel$, $(|\underset{\sim}{B}|/B_\infty)_\perp$, and $(B/B_\infty)_n$ in the rotated system are next determined by bilinear interpolation through the flow field grid. Then the magnetic field components (B'_x, B'_y, B'_z) in the rotated system are calculated from

$$\begin{aligned} B'_x = \cos\alpha'_n \Bigg[&\cos\phi \cdot \cos\alpha'_p \cdot \left|\frac{\underset{\sim}{B}}{B_\infty}\right|_\parallel \\ &+ \cos\psi \cdot \sin\alpha'_p \cdot \left|\frac{\underset{\sim}{B}}{B_\infty}\right|_\perp \Bigg] \cdot B_\infty \end{aligned} \tag{56}$$

$$\begin{aligned} B'_y = \cos\alpha'_n \Bigg[&\sin\phi \cdot \cos\alpha'_p \cdot \left|\frac{\underset{\sim}{B}}{B_\infty}\right| \\ &+ \sin\psi \cdot \sin\alpha'_p \cdot \left|\frac{\underset{\sim}{B}}{B_\infty}\right|_\perp \Bigg] \cdot B_\infty \end{aligned} \tag{57}$$

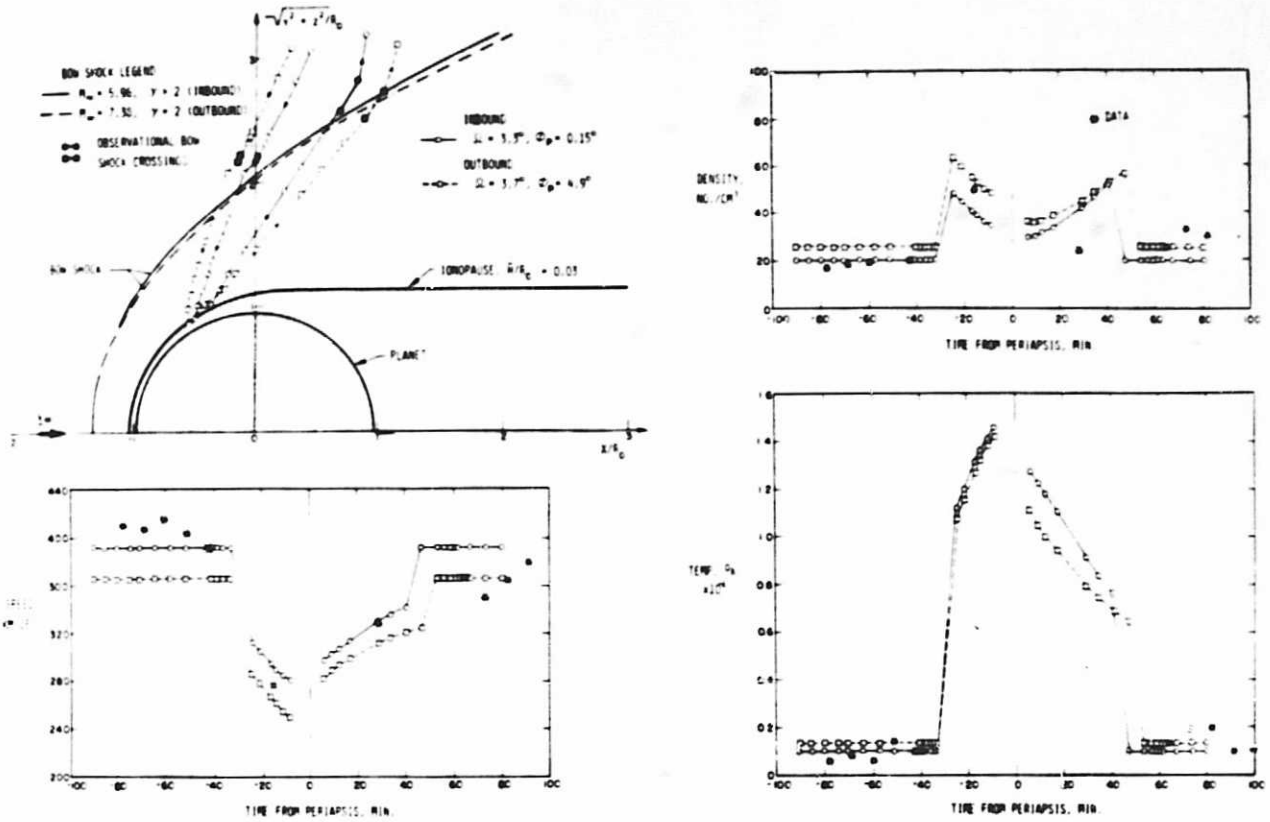

Fig. 15. Comparison of observed and theoretical time histories of ionosheath plasma properties for Pioneer Venus orbit 3 based on inbound and outbound interplanetary solar wind conditions.

$$B_z' = \sin\alpha_n' \cdot \left(\frac{B}{B_\infty}\right)_n \cdot B_\infty \tag{58}$$

The magnetic field components in the solar wind (X, Y, Z) system are then determined from the rotational transformation

$$\begin{pmatrix} B_X \\ B_Y \\ B_Z \end{pmatrix} = \begin{pmatrix} 1 & 0 & 0 \\ 0 & \cos\theta & -\sin\theta \\ 0 & \sin\theta & \cos\theta \end{pmatrix} \begin{pmatrix} B_x' \\ B_y' \\ B_z' \end{pmatrix} \tag{59}$$

and finally in the sun-planet system from

$$\begin{pmatrix} B_{x_s} \\ B_{y_s} \\ B_{z_s} \end{pmatrix} \begin{pmatrix} -\cos\Omega\cos\phi_p & \sin\Omega & -\cos\Omega\sin\phi_p \\ \sin\Omega\cos\phi_p & -\cos\Omega & \sin\Omega\sin\phi_p \\ \sin\phi_p & 0 & \cos\phi_p \end{pmatrix} \begin{pmatrix} B_X \\ B_Y \\ B_Z \end{pmatrix} \tag{60}$$

Results

Using the computational procedures described above, a large number of solutions have been calculated for a wide variety of conditions representative of those that might be experienced at Venus. A sample of these results is illustrated in Figure 9 for $M_\infty = 8$, $\gamma = 5/3$, and $\bar{H}/R_O = 0.10$ with B_∞ either parallel or perpendicular to V_∞. These and similar determinations for the following 35 other sets of conditions have been included in a catalog of results available from Stahara et al. [1980]:

M_∞ = (2.0, 3.0, 5.0, 8.0, 12.0, 25.0)

H/R_O = (0.01, 0.10, 0.25)

$\bar{H}/R_O$ = (0.10, 0.20, 0.25)

Also included in that reference are a few results for conditions well outside the range likely to be encountered at Venus but that are useful because they illustrate the extended capability of the present procedures.

Verification of the new procedures has been done in a variety of ways in addition to comparison with previous results for sets of conditions for which both sets of results could be determined. These include consideration of a variety of special test cases in which the location in the flow field and the incident interplanetary magnetic field orientation were systematically changed so as to produce both symmetric and antisymmetric changes in the resultant ionosheath magnetic field, as well as to reverse the roles of the perpendicular and normal components. All of these various permutations of the magnetic field calculations were successfully verified.

The final and ultimate check of the theoretical

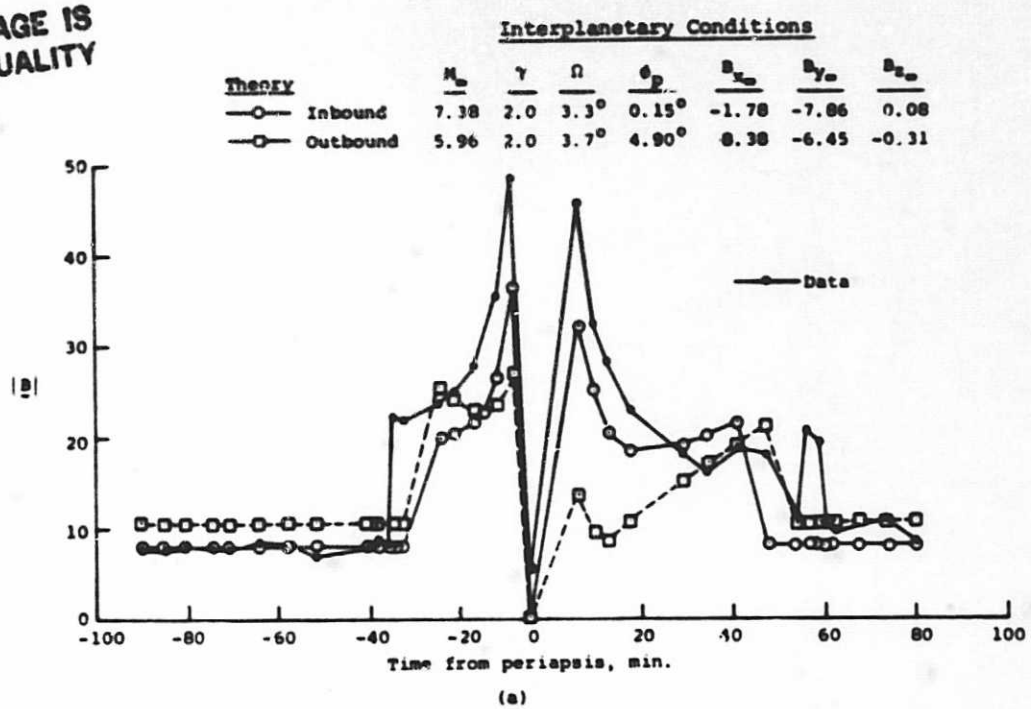

Fig. 16. Comparison of observed (OMAG) and theoretical time histories for the magnetic field for Pioneer Venus orbit 3 based on inbound and outbound interplanetary solar wind conditions using gasdynamic solutions $M_\infty = 7.38$, $\gamma = 2.0$ for inbound and $M_\infty = 5.96$, $\gamma = 2.0$ for outbound calculations. (a) Magnetic field magnitudes. (b) Magnetic field components.

model and numerical procedures lies in the comparison of the predicted results with data actually measured by a spacecraft. Attention is now turned, accordingly, to the results of preliminary comparisons with data obtained from orbits 3 and 6 of the Pioneer-Venus orbiter. These orbits were selected in conjunction with the experimenters on the basis of completeness of data and apparent steadiness of conditions during the time of interest for the study.

To perform calculations suitable for comparison with data from a particular orbit, it is necessary to specify appropriate conditions corresponding to those actually measured in both the ionosphere and in the oncoming interplanetary solar wind plasma. On the basis of data from the orbiter retarding potential analyzer (OPRA) indicating the ionospheric scale height to be approximately 200 km for orbits 3 and 6, a value of 0.03 was selected for H/R_0 or $\bar{H}/R_0$. For such small values the two ionospheric pressure models indicated by (20) and (21) yield essentially the same obstacle shape, as can be seen from Figure 2. With regard to oncoming interplanetary conditions it is required that values for the solar wind bulk velocity $\underline{v}_\infty$, density ρ_∞, temperature T_∞, and magnetic field $\underline{B}_\infty$ be specified. The first three are provided by the orbiter plasma analyzer (OPA), and the magnetic field is given by the orbiter flux gate magnetometer (OMAG). OPA provides either ion or electron data, but not both simultaneously. For orbits 3 and 6, ion measurements were available and have been employed. Data on the oncoming direction of the solar wind, as given in terms of the angles (Ω, ϕ_p), define the coordinate rotations required to align the gasdynamic calculation in the free-stream solar wind direction; while information of solar wind speed, density, and temperature serve to define the free-stream gasdynamic Mach number M_∞.

Although it is known the temperatures of the ions and electrons may be substantially different in the solar wind plasma (a ratio $T_e/T_i \sim 4$ is often representative), they are assumed to be equal ($T_e/T_i = 1$) in the derivation of the single-fluid magnetohydrodynamic equations upon which the present calculations are based. Now that the theory has been put into a more readily usable form and more extensive data on the temperature of both electrons and ions are becoming available for comparative studies, steps should be taken to improve understanding of the relation between single- and multiple-component plasma theories for space plasma flows, and the calculative procedures refined as appropriate.

With this information the detailed gasdynamic and unit magnetic field calculations in the ionosheath region can be carried out. To provide an idea of the detail obtained by the present computational procedures, Figure 10 displays the flow field grid for one of the gasdynamic solutions used in the comparisons. Values for each of the plasma properties $\underline{v}/v_\infty$, ρ/ρ_∞, T/T_∞, $(\underline{B}/B_\infty)_n$, $(\underline{B}/B_\infty)_\perp$ and $(B/B_\infty)_n$ are determined at each intersection of the grid lines, including the bow shock, stagnation streamline, and ionopause boundary. The final output of the calculation consists of these quantities and the coordinates of the bow shock and ionopause, expressed either in tabular form or as plotted contours, and also as time histories along a specified trajectory.

For comparisons with spacecraft data the time-

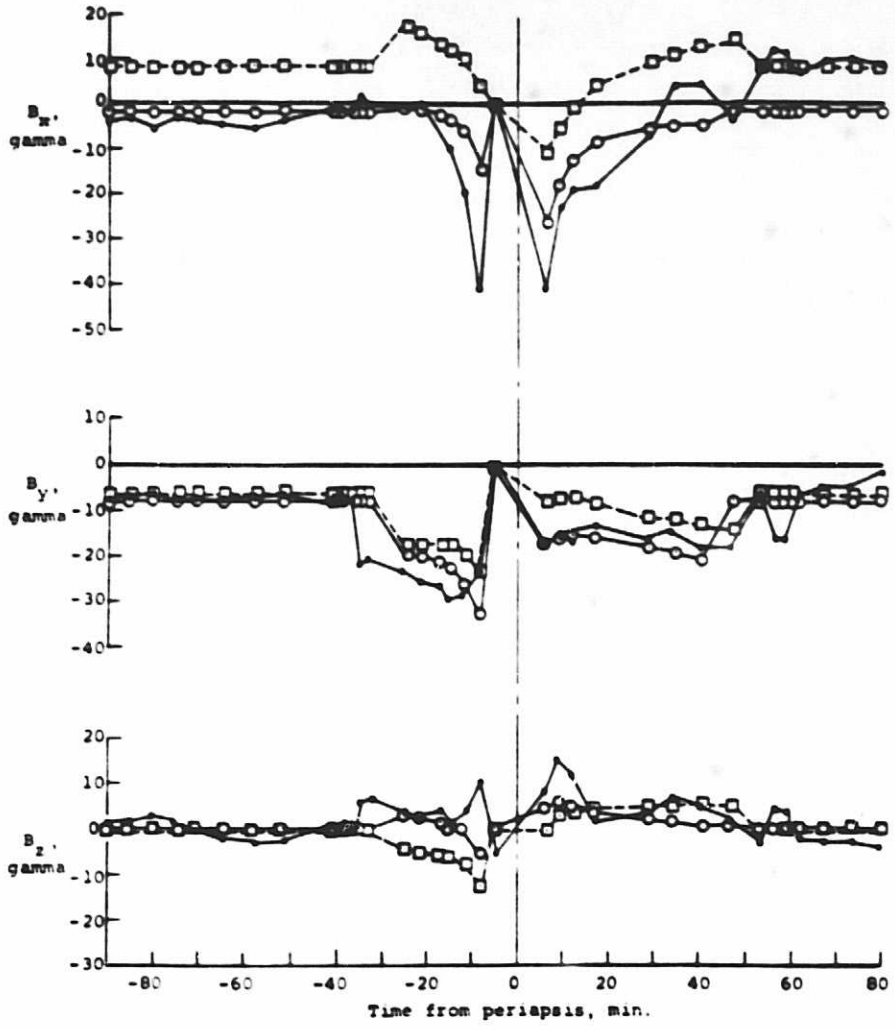

(b)

Fig. 16. (continued)

history predictions are the most convenient. For the theoretical predictions, two sets of results are usually generated on the basis of the last/first interplanetary solar wind properties measured before/after bow shock inbound/outbound crossing.

Figure 11 displays some overall flow field results for orbit 6. Indicated are bow shock locations for the three combinations of M_∞ and plasma specific heat ratio γ, i.e., (M_∞, γ) = (13.3, 5/3), (13.3, 2), (3.0, 5/3) for flow about an ionopause with $\bar{H}/R_0 = 0.03$. Also indicated are two sets of points (solid lines with circles, and dashed lines with squares) representing the spacecraft trajectory as viewed in two solar wind oriented coordinate systems. The trajectory indicated by the solid lines and circles is that based on the last measured direction (Ω, ϕ_p) = (6.5°, -1.4°) of the interplanetary solar wind just prior to crossing the bow shock on the inbound leg, while the dashed lines and squares denote the trajectory based on the first measured direction (Ω, ϕ_p) = (4.9°, 7.6°) of the solar wind immediately after crossing the bow shock on the outbound leg. These results illustrate the extremely large dependence of spatial position of a trajectory point, as viewed in solar wind coordinates, on solar wind direction. For the particular angles indicated, the shift in X coordinate of a trajectory point can be as great as a quarter of the Venusian planetary radius and obviously results in substantial differences in predicted flow and magnetic field properties. Although Spreiter and Rizzi [1972] noted the importance of such an effect in the interpretation of the data from Mariner 4 in its flyby of Mars, the effects of angular shifts in the solar wind direction are usually ignored in most discussions of the interaction. The present results, however, indicate that this purely geometrical effect can be very significant, even for directional shifts of less than 5°, and must be accounted for in any quantitative comparison of theoretical and observational results.

The selection of values for M_∞ and γ in Figure 11 represents an attempt to resolve the uncertainty in the appropriate values for these parameters. Because only solar wind ion temperatures from the OPA were available for orbit 6, the initial calculations of M_∞ were based on the assumptions that $T_e = T_i$, which leads to $M_\infty = 13.3$ and $\gamma = 5/3$, as appropriate for a gas with parti-

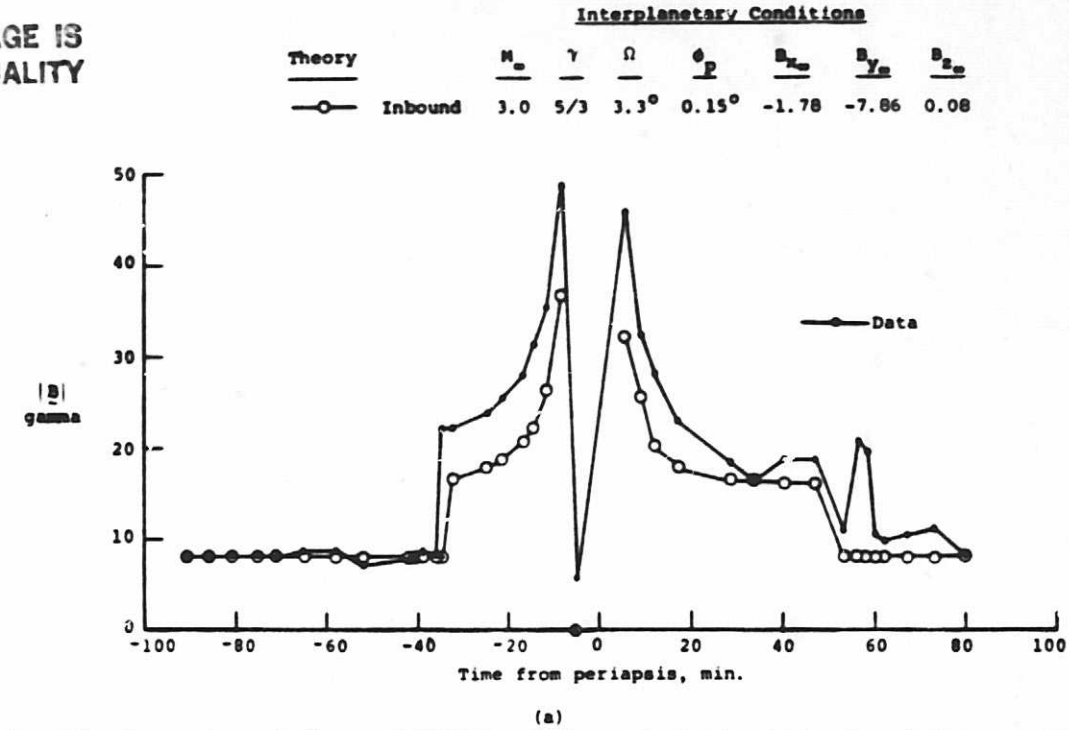

Fig. 17. Comparison of observed (OMAG) and theoretical time histories of the magnetic field for Pioneer Venus orbit 3 based on inbound solar wind interplanetary conditions using a gasdynamic solution for $M_\infty = 3.0$, $\gamma = 5/3$. (a) Magnetic field magnitude. (b) Magnetic field components.

cles possessing 3 degrees of freedom for their molecular motion. The resulting location for the shock wave is not in good agreement with the observations. To investigate whether changing the value for γ to 2, which corresponds to a gas with 2 degrees of freedom as might be supposed to occur if the magnetic field sufficiently aligns the molecular motion, the calculations were repeated with $M_\infty = 13.3$ and $\gamma = 2$. The results, indicated by the dashed line, are in improved, but still not completely satisfactory, agreement with the observed shock locations. Finally, if it is assumed that the oncoming interplanetary electron temperature is not equal to the ion temperature but is substantially higher, we are led to consider low values of the order of 3-5 for M_∞. Results for $M_\infty = 3.0$, $\gamma = 5/3$ are indicated in Figure 11 by the solid line. It may be seen that results calculated for these values and for the inbound solar wind direction are in very good agreement with the theoretical results. These comparisons make evident both the possibilities and the uncertainties in the use of the theory at the present level of understanding of the parameter selection process.

Figure 12 displays the time history comparisons of the predicted bulk plasma density, speed, and temperature with OPA data. The solid lines with circles correspond to results based on inbound interplanetary conditions, while the dashed lines with squares correspond to outbound conditions. While the one data point in the ionosheath for each quantity is in general agreement with the theoretical calculation, the lack of more detailed plasma data prevents a definitive conclusion. The OPA requires approximately 9 min to acquire sufficient data to enable determination of the bulk plasma quantities. This time interval usually presents no problem when the spacecraft is in the interplanetary solar wind, but the large resolution time effectively averages the plasma quantities in the ionosheath over such a large spatial range that only overall comparisons of the bulk plasma properties are possible with this instrument.

The situation is quite different for the magnetic field, since the OMAG provides essentially instantaneous measurements. Figure 13 displays a comparison of the data from orbit 6 with two sets of theoretical results based on the inbound and outbound interplanetary conditions. In these comparisons both sets of predictions exhibit good agreement with the data for the appropriate part of the trajectory. Thus, on the inbound leg the predictions based on the inbound interplanetary conditions are in good agreement with the data, while the outbound-condition predictions are notably inferior, particularly with regard to shock crossing; and conversely. Since steadiness of the interplanetary conditions was a criterion used in the selection of orbit 6 for these comparisons, the results of Figure 13 serve to illustrate the need for simultaneous measurements of interplanetary conditions and planetary flow field conditions in more definitive evaluations of the theory.

Results for corresponding comparisons for orbit 3 are given in Figures 1[illegible], and 16. In Figure 14, bow shock location[illegible] presented for five different combinations of M_∞ and γ. The Mach numbers $M_\infty = 7.38$ and 5.96 correspond to the inbound and outbound interplanetary conditions,

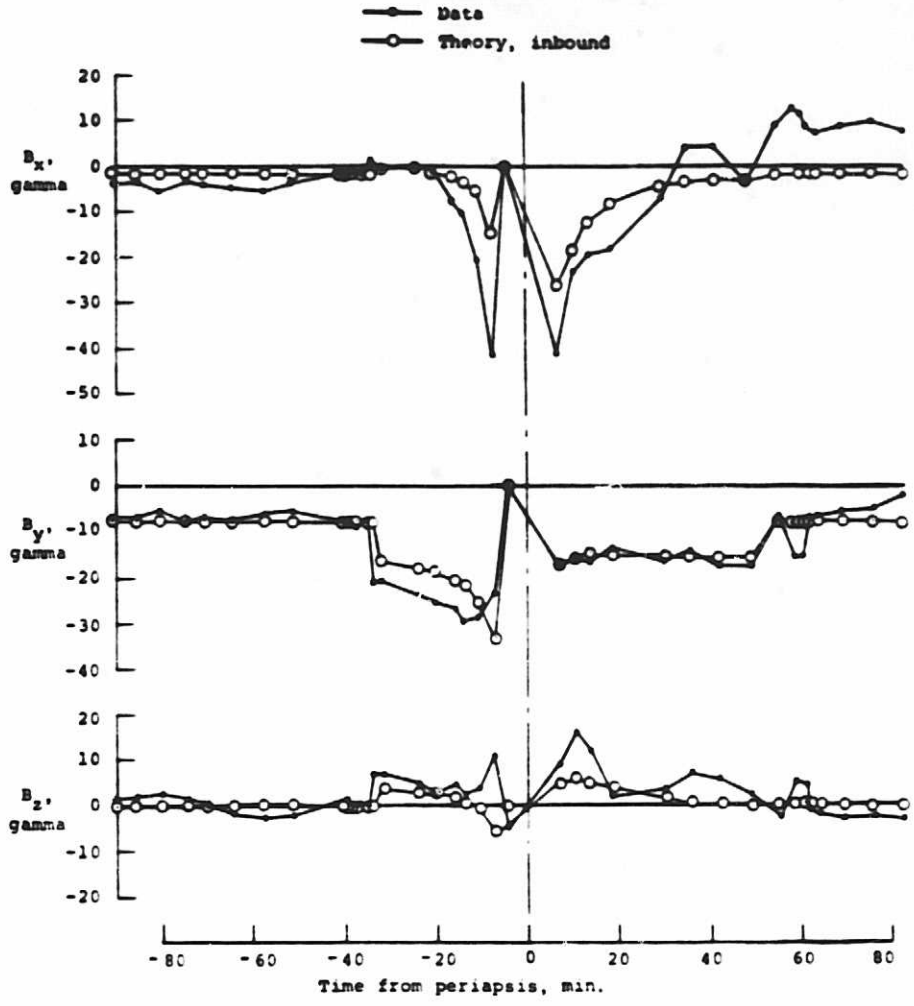

(b)

Fig. 17. (continued)

respectively, for $|v_\infty|$, ρ_∞, and T_∞ as measured for the ions by the OPA; the two values for $\gamma = 5/3$, 2 are indicative of present uncertainty about the effective ratio of specific heats for the solar wind plasma. The bow shock location for $M_\infty = 3$ and $\gamma = 5/3$ given previously in Figure 11 for orbit 6 is also included, because once again it is closer to the observed shock crossings. Also provided in Figure 14 are the orbital trajectories as viewed in solar wind coordinates for the inbound $(\Omega, \phi_p) = (3.3°, 0.15°)$ and outbound $(\Omega, \phi_p) = (3.7°, 4.9°)$ solar wind directions.

The comparisons for the bulk plasma properties for orbit 3 shown in Figure 15 are marked again by the paucity of observational data. What information there is suggests agreement for the plasma speed and density but a notable discrepancy for the temperature. This is thought to be indicative of the manner in which the bulk properties from the theoretical model are interpreted in relation to the observational measurements; i.e., the theoretical values correspond to those for a single-component plasma in which it is considered that the electrons and ions have equal temperatures, whereas the measurements are for the ions only in a multicomponent plasma in which the ion and electron temperatures are usually quite different. A more penetrating analysis of the meaning of the temperature in the theory and its relation to that deduced by the experimenters from their data appears to be a necessary and important subject for future study.

Results for the magnetic field comparisons are displayed in Figure 16, which provides time histories of the magnitude and individual components based on both inbound and outbound interplanetary conditions. Although the shock crossings are somewhat in disagreement, since the calculated results are for $M_\infty = 7.56$, 6.96 and $\gamma = 2$, the general trends displayed by the calculated and observed results are notably similar, particularly if account is taken of the drift with time along the trajectory of the transition from the calculations based on inbound conditions to ones based on the outbound conditions.

To demonstrate the improvement obtained in magnetic-field results when a gasdynamic flow field solution is employed which more closely agrees with the observational bow shock location, the magnetic field time histories from orbit 3 are compared in Figure 17 using gasdynamic results for $M_\infty = 3.0$, $\gamma = 5/3$, and the directions $(\Omega, \phi_p) =$

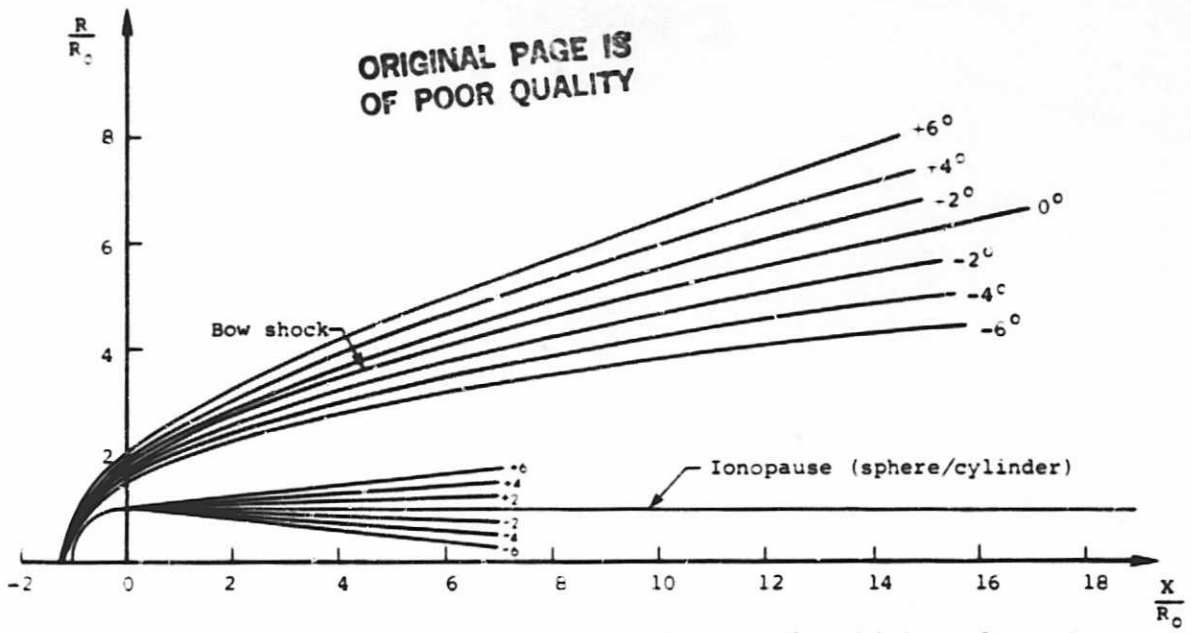

Fig. 18. Illustration of effect on bow shock location of variability of oncoming solar wind direction; $M_\infty = 8.0$, $\gamma = 5/3$ flow past a sphere/cylinder ionopause obstacle.

(3.3°, 0.15°) measured at the inbound shock crossing. As can be seen, there is a marked improvement in the agreement near the bow shock and quite good agreement throughout the ionosheath for both the magnitude and the individual magnetic field components. In addition to illustrating again that further study needs to be made of the parameter selection process required to relate the calculated and observational results optimally, these comparisons emphasize once again the need to account in the calculations for the actual direction of the interplanetary solar wind flow.

To illustrate the significance of this point, Figure 18 has been prepared to show that even a modest change of ±6° in the direction of the incident solar wind can have substantial effects on the location of the ionopause and bow wave, as viewed in a coordinate system aligned with the Sun-Venus direction which is typical of most presentations of observational data. It would be of considerable interest to determine how much of the scatter of data for the location of the bow wave may be attributable to this simple factor.

A further point of growing concern is associated with effects of significant changes downstream of the terminator of the ionopause shape from that calculated herein. More detailed comparisons will have to be reserved for future studies, but the results of Figure 19 for the theoretical characteristic lines emanating from the intersection of the ionopause and the terminator define the region of influence of a small inward or outward taper of the ionopause profile downstream of the terminator. For the entire region displayed extending downstream to more than 16 Venus radii, these results indicate that there is no accompanying change in the location of the bow wave. It may also be noted that the point designated by number 2 in the Mariner 5 data from Venus (see Spreiter and Alksne [1970] for an earlier comparison with theory), where the ionosheath plasma changes from comparatively quiet to disturbed, is remarkably close to the characteristic line from the terminator. Such behavior could result from unsteady fluctuations of the ionopause surface beginning approximately at the terminator. The data from Pioneer Venus should be examined to determine whether this is a general property of the plasma in the vicinity of these characteristic lines or perhaps just the result of some passing transient occurring at the time of the Mariner 5 encounter.

Concluding Remarks

The present application of advanced computational procedures to the modeling of solar wind flow past Venus was undertaken to improve the accuracy and utility of the theoretical predictions. Starting with the steady, dissipationless, magnetohydrodynamic model for axisymmetric, supersonic, super-Alfvénic solar wind past a nonmagnetic planet with a shielding ionosphere, a number of important theoretical extensions have been developed and implemented. These include the capability for treating lower interplanetary gasdynamic Mach numbers M_∞ down to about 2 and a wider variety of ionopause shapes including a new family of shapes which includes the effect of gravitational variation in the scale height. Additionally, the capability for determining the plasma gasdynamic and magnetic field properties along any arbitrary trajectory, accounting for an arbitrary oncoming direction of the solar wind, has been established. All of these developments have been incorporated into a current computational model to enable detailed calculations of the solar wind interaction with Venus. The model has been comprehensively described by Stahara et al. [1980]. Also included in that account is an extensive catalog of results for a wide range of flow conditions and ionopause shapes representative of those that might be anticipated at Venus or at

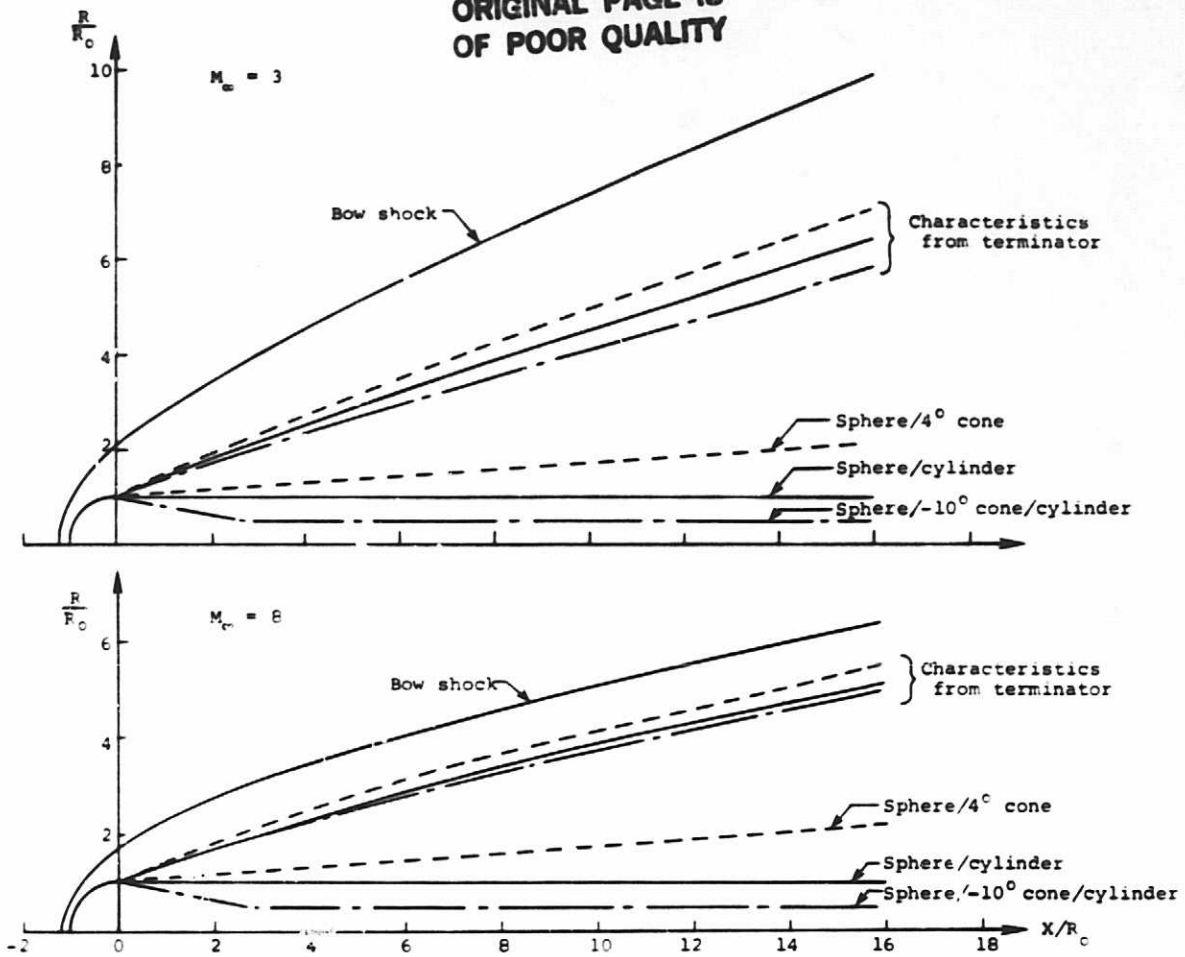

Fig. 19. Illustration of effect of various wake shapes on bow shock location and characteristics from terminator; $\gamma = 5/3$, $M_\infty = 3$ and 8.

some other nonmagnetic planet with a shielding ionosphere.

Finally, theoretical results determined from the model have been compared with data from two of the early orbits of the Pioneer Venus orbiter. These comparisons have indicated the importance, heretofore largely neglected, of the directional variability of the oncoming solar wind. These results, taken in toto, serve to verify the basic theoretical model and the effectiveness of the numerical solution, although it is evident that further study should be applied to certain questions relating to interpretation of plasma quantities like the temperature. The results demonstrate also the value of the present theoretical procedures as a research tool capable of routinely providing--at small computational cost and in a form directly compatible with observations--details of the solar wind/planetary atmosphere interaction process not previously attainable.

With regard to future uses as well as improvements of the present model, the obvious need for a detailed study involving comparison between theory and observations for a large number of orbits of the Pioneer Venus orbiter is clear. On the basis of the preliminary comparisons for orbits 3 and 6 the calculated magnetic field appears to be remarkably accurate for relatively quiettime conditions. Similar comparisons of the plasma properties indicate a need for an improved interpretation of the results from the single-fluid theory in terms of multicomponent measurements. Questions regarding the possible suppression by the interplanetary magnetic field of the number of degrees of freedom of the plasma require further study and could be clarified through systematic comparisons with data. Additionally, observations from the Pioneer Venus orbiter of the nightside ionosphere of Venus have revealed a more complex and dynamic structure than suspected. These observations point, in particular, toward the need for improvement of the simple model used in the present method for the determination of the ionosphere boundary downstream of the terminator. This improved determination would involve an iterative procedure in which a balance of the sum of the solar wind gasdynamic and magnetic pressures along the ionopause surface would be maintained against the ionospheric pressure, not necessarily assumed to be spherically symmetric. The present method, which balances the extended Newtonian gas plus magnetic pressure distribution against the ionospheric pressure, might represent the first step of such an iteration; but it is also possible that dynamic effects associated with intermittently passing volumes of magnetized plasma torn from more upstream regions

of the ionopause might greatly impair the general utility of any stationary model for the ionopause downstream of the terminator. This is another important topic awaiting further study.

Acknowledgments. Support for the research reported here was provided by the National Aeronautics and Space Administration, Headquarters, under contracts NASW-3182 and NASW-3184. Special thanks are due to J. H. Wolfe and J. P. Mihalov, who provided solar wind plasma data from the OPA [Wolfe et al., 1979; Intriligator et al., 1979]; to C. T. Russell, R. C. Elphic, and J. A. Slavin, who provided magnetic field data from the OMAG [Russell et al., 1979a, b]; and to W. C. Knudsen and K. Spenner, who provided ionospheric plasma data from the ORPA [Knudsen et al., 1979a, b].

The Editor thanks R. C. Elphic and E. W. Greenstadt for their assistance in evaluating this paper.

References

Alksne, A. Y., and D. L. Webster, Magnetic and electric fields in the magnetosheath, Planet. Space Sci., 18, 1203-1212, 1970.

Beam, R. M. and R. F. Warming, An implicit finite-difference algorithm for hyperbolic systems in conservation-law form, J. Comput. Phys., 22, 87-110, 1976.

Brace, L. H., H. A. Taylor, Jr., P. A. Cloutier, R. E. Daniell, Jr., and A. F. Nagy, On the configuration of the nightside Venus ionopause, Geophys. Res. Lett., 6, 345-348, 1979.

Brace, L. H., R. F. Theis, W. R. Hoegy, J. H. Wolfe, C. T. Russell, R. C. Elphic, and A. F. Nagy, The dynamic behavior of the Venus ionosphere in response to solar wind interactions, J. Geophys. Res., this issue.

Chaussee, D. S., T. Holtz, and P. Kutler, Inviscid supersonic/hypersonic body flow fields and aerodynamics from shock-capturing technique calculations, Pap. 75-837, Amer. Inst. of Aeronaut. and Astronaut., New York, 1975.

Dryer, M., and R. Faye-Petersen, Magnetogasdynamic boundary condition for a self-consistent solution to the closed magnetopause, AIAA J., 4, 246-254, 1966.

Dryer, M., and G. R. Heckman, Application of the hypersonic analogy to the standing shock of Mars, Solar Phys., 2, 112-120, 1967.

Intriligator, D. S., H. R. Collard, J. P. Mihalov, R. C. Whitten, and J. H. Wolfe, Electron observation and ion flows from the Pioneer-Venus Orbiter plasma analyzer experiment, Science, 205, 116-119, 1979.

Kentzer, C. P., Discretization of boundary conditions on moving discontinuities, Proceedings of the Second International Conference on Numerical Methods in Fluid Dynamics, Lect. Notes Phys., 8, 108-113, 1970.

Knudsen, W. C., K. Spenner, J. R. Spreiter, K. L. Miller, and V. Novak, Thermal structure and major ion composition of the Venusian ionosphere: First RPA results from Venus Orbiter, Science, 203, 757-763, 1979a.

Knudsen, W. C., K. Spenner, R. C. Whitter, J. R. Spreiter, K. L. Miller, and V. Novak, Thermal structure and energy influx to the day- and nightside Venus ionosphere, Science, 205, 105-107, 1979b.

Kutler, P., W. A. Reinhardt, and R. F. Warming, Numerical computations of multi-shocked three-dimensional supersonic flow fields with real gas effects, Pap. 72-702, Amer. Inst. of Aeronaut. and Astronaut., New York, 1972.

Kutler, P., W. A. Reinhardt, and R. F. Warming, Multi-shocked, three-dimensional supersonic flow fields with real gas effects, AIAA J., 11, 657-664, 1973.

MacCormak, R. W., The effect of viscosity in hypervelocity impact cratering, Pap. 69-354, Amer. Inst. of Aeronaut. and Astronaut., New York, 1969.

Russell, C. T., R. C. Elphic, and J. A. Slavin, Initial Pioneer Venus magnetic field results: Dayside observations, Science, 203, 745-748, 1979a.

Russell, C. T., R. C. Elphic, and J. A. Slavin, Initial Pioneer Venus magnetic field results: Nightside observations, Science, 205, 114-116, 1979b.

Spreiter, J. R., Magnetohydrodynamic and gasdynamic aspects of solar-wind flow around terrestrial planets: A critical review, NASA Spec. Publ., SP-397, 135-150, 1976.

Spreiter, J. R., and A. Y. Alksne, Solar wind flow past objects in the solar system, Annu. Rev. Fluid Mech., 8, 313-354, 1970.

Spreiter, J. R., and W. P. Jones, On the effect of a weak interplanetary magnetic field on the interaction between the solar wind and the geomagnetic field, J. Geophys. Res., 68, 3555-3564, 1963.

Spreiter, J. R., and A. W. Rizzi, Aligned magnetohydrodynamics solution for solar wind flow past the earth's magnetosphere, Acta Astronaut., 1, 15-35, 1974.

Spreiter, J. R., A. Y. Alksne, and A. L. Summers, Hydromagnetic flow around the magnetopause, Planet. Space Sci., 14, 223-253, 1966.

Spreiter, J. R., A. Y. Alksne, and A. L. Summers, External aerodynamics of the magnetosphere, in Physics of the Magnetosphere, edited by R. L. Carovillano, J. F. McClay, and H. R. Radoski, pp. 304-378, D. Reidel, Hingham, Mass., 1968.

Spreiter, J. R., A. L. Summers, and A. W. Rizzi, Solar wind flow past nonmagnetic planets - Venus and Mars, Planet. Space Sci., 18, 2181-2189, 1970.

Stahara, S. S., D. S. Chaussee, B. C. Trudinger, and J. R. Spreiter, Computational techniques for solar wind flows past terrestrial planets - Theory and computer programs, NASA Contract. Rep., CR-2924, 1977.

Stahara, S. S., D. Klenke, B. C. Trudinger, and J. R. Spreiter, Application of advanced computational procedures for modeling solar-wind interactions with Venus - Theory and computer code, NASA Contract. Rep., CR-3267, 1980.

Thomas, P. D., M. Vinokur, R. Bastionon, and R. J. Conti, Numerical solution for the three-dimensional hypersonic flow field of a blunt delta body, AIAA J., 10, 887-894, 1972.

Wolfe, J., D. S. Intriligator, J. Mihalov, H. Collard, D. McKibbin, R. Whitten, and A. Barnes, Initial observations of the Pioneer Venus Orbiter solar wind plasma experiment, Science, 203, 750-752, 1979.

(Received February 2, 1980;
revised April 4, 1980;
accepted April 7, 1980.)